AGU PUBLICATIONS

JGR

Journal of Geophysical Research: Solid Earth

RESEARCH ARTICLE
10.1002/2017JB014265

Key Points:
- We combine two important source observational methods to constrain and infer the rupture dynamics of megathrust earthquakes
- We present the spatial and temporal evolution of earthquake dynamics during the 2015 M_w 8.3 Illapel earthquake
- Our methodologies are an attempt to bridge kinematic observations with earthquake dynamics

Supporting Information:
- Supporting Information S1
- Figure S1
- Movie S1

Correspondence to:
J. Yin,
jiuxun_yin@g.harvard.edu

Citation:
Yin, J., Denolle, M. A., & Yao, H. (2018). Spatial and temporal evolution of earthquake dynamics: Case study of the M_w 8.3 2015 Illapel Earthquake, Chile. *Journal of Geophysical Research: Solid Earth*, *123*. https://doi.org/10.1002/2017JB014265

Received 31 MAR 2017
Accepted 5 DEC 2017
Accepted article online 13 DEC 2017

Spatial and Temporal Evolution of Earthquake Dynamics: Case Study of the M_w 8.3 Illapel Earthquake, Chile

Jiuxun Yin[1], Marine A. Denolle[1], and Huajian Yao[2]

[1]Department of Earth and Planetary Sciences, Harvard University, Cambridge, MA, USA, [2]Laboratory of Seismology and Physics of Earth's Interior and School of Earth and Space Sciences, University of Science and Technology of China, Hefei, China

Abstract We develop a methodology that combines compressive sensing backprojection (CS-BP) and source spectral analysis of teleseismic *P* waves to provide metrics relevant to earthquake dynamics of large events. We improve the CS-BP method by an autoadaptive source grid refinement as well as a reference source adjustment technique to gain better spatial and temporal resolution of the locations of the radiated bursts. We also use a two-step source spectral analysis based on (i) simple theoretical Green's functions that include depth phases and water reverberations and on (ii) empirical *P* wave Green's functions. Furthermore, we propose a source spectrogram methodology that provides the temporal evolution of dynamic parameters such as radiated energy and falloff rates. Bridging backprojection and spectrogram analysis provides a spatial and temporal evolution of these dynamic source parameters. We apply our technique to the recent 2015 M_w 8.3 megathrust Illapel earthquake (Chile). The results from both techniques are consistent and reveal a depth-varying seismic radiation that is also found in other megathrust earthquakes. The low-frequency content of the seismic radiation is located in the shallow part of the megathrust, propagating unilaterally from the hypocenter toward the trench while most of the high-frequency content comes from the downdip part of the fault. Interpretation of multiple rupture stages in the radiation is also supported by the temporal variations of radiated energy and falloff rates. Finally, we discuss the possible mechanisms, either from prestress, fault geometry, and/or frictional properties to explain our observables. Our methodology is an attempt to bridge kinematic observations with earthquake dynamics.

1. Introduction

The largest earthquakes in recorded history, such as the 2004 Sumatra M_w 9.2, the 1960 Great Chilean M_w 9.4, the 1964 Alaskan M_w 9.3, and the 2011 Tohoku M_w 9.0 megathrust earthquakes, have killed many, caused great damage, and brought tremendous financial losses. These earthquakes induce not only strong ground motion but also large tsunami waves. As coastal populations grow, mitigating the earthquake risk is critical. However, the remoteness of megathrust earthquakes limits the near-field instrumentation and we are left with using teleseismic measurements to infer the source processes and hazards when such an earthquake occurs. The development of geophysical instrumentations along with that of array processing techniques provides us tools to harness more information from teleseismic data and to better characterize the source processes.

The slip inversion on the fault is a classic approach to construct a static and/or kinematic description of the earthquake rupture (e.g., Ji et al., 2002a, 2002b; Kikuchi & Kanamori, 1982, 1986, 1991). Static slip inversions yield the total slip that occurred during the earthquake and may be obtained from low-frequency seismic waves and/or geodetic measurements. Kinematic slip inversions solve for the time evolution of slip on the fault. They often require higher-frequency seismic waves and/or high-rate GPS data and often necessitate assumptions of the earthquake dynamics by imposing the slip rate functional shape. Furthermore, these inversions are particularly nonunique (Mai et al., 2016), require regularization, and thus yield different estimations of peak value and location of the maximum slip. Finally, as slip models can provide important estimates of static stress drop, the regularization in the inversion directly affects the values (e.g., Brown et al., 2015; Yin et al., 2016).

Backprojection of high-frequency (0.08–4 Hz) teleseismic *P* waves is another method widely used to study the evolution of earthquake radiation and is particularly effective for large earthquakes. With the development of

dense seismic array (e.g., Hi-net in Japan (Anon, 2005; Okada et al., 2004); USArray (*Earthscope program*)), we can harness key information from waveform coherency through the approximation that the Green's function is identical within the seismic array except for phase delays. The backprojection can directly provide the distribution of seismic energy bursts (Ishii et al., 2005, 2007) provided that we can stack the waveforms (or complex spectra) coherently through travel time/phase shifting. Its application to the recent large earthquakes ($M_w > 8$) has succeeded in characterizing the spatiotemporal evolution of seismic radiation (Fan & Shearer, 2016; Ishii et al., 2005, 2007; Kiser et al., 2011; Meng et al., 2011; Xu et al., 2009; Yagi & Okuwaki, 2015; Yao et al., 2011, 2012; Yin et al., 2016). Backprojection methods require fewer assumptions than slip inversions. Therefore, preliminary information about earthquake rupture process can be rapidly obtained from waveform data after the waves arrive at the seismic array (e.g., Incorporated Research Institutions for Seismology Data Management Center (IRIS DMC), 2011).

If we are to interpret the backprojection results in terms of earthquake dynamics, understanding rigorously their relation is critical. Theoretical studies indicate that the high-frequency seismic waves can be excited during abrupt changes in rupture velocity (Bernard & Madariaga, 1984; Madariaga, 1977; Spudich & Frazer, 1984) caused either by the arrest of the rupture (Madariaga, 1976) or by kinks of the fault geometry (Madariaga et al., 2006). Moreover, Fukahata et al. (2014) propose that the backprojection images are equivalent to either slip or slip rate on the fault, provided that the Green's functions from the sources to the receivers are incoherent delta functions. Huang et al. (2012, 2014) introduce frictional heterogeneity on the fault surface to reproduce the excitation of high-frequency radiators at depth. Backprojection thus shows promise to provide observational constraints and information about the earthquake dynamics, in together with other independent techniques.

To complement efforts inferring earthquake dynamics from slip inversions and backprojection, we turn to source spectral analysis and quantify the amount of seismic energy radiated at the source. Through model fitting (Aki, 1967; Boatwright, 1980; Brune, 1970, 1971; Eshelby, 1957; Haskell, 1964; Madariaga, 1976), source spectral analysis has been a popular method to provide estimates of static and dynamic source parameters such as static stress drop (with measure of the corner frequency interpreted as source duration and the assumption of a uniform stress drop on a crack), radiated energy (with measures of velocity amplitude spectra). Radiation efficiency, a measure of energy partitioning, can be obtained from the ratio of radiated energy with static stress drop (Husseini, 1977; Ko & Kuo, 2016; Poli & Prieto, 2016; Venkataraman & Kanamori, 2004; Ye et al., 2016). Additional information such as measures of high-frequency falloff rate n brings insight to the efficiency or deficiency in high-frequency excitation (Aki, 1967; Haskell, 1964; Kaneko & Shearer, 2014; Madariaga, 1977).

In this study, we build from Denolle et al. (2015) and by rigorously combining the two independent observational methods, backprojection and spectral analysis, to evaluate the evolution in time and in space of dynamic source parameters.

The first method is an Improved Compressive Sensing Backprojection method, which we refer to as ImCS-BP herein. The original CS-BP method (Yao et al., 2011; Yin & Yao, 2016) uses a frequency domain formulation of the conventional backprojection method by extracting the phase coherence between velocity seismograms recorded at seismic arrays. CS-BP can locate the seismic energy bursts with high spatial resolution based on sparsity-constrained inversion (Yao et al., 2011; Yin & Yao, 2016). Here we increase the spatial resolution and improve the computational efficiency to provide better accuracy and precision on the spatiotemporal evolution of seismic energy bursts.

Second, we complement the phase information provided by backprojection with the amplitude information provided by *P* wave source spectrogram analysis. Our methodology also allows us to estimate *P* wave radiated energy and to parameterize the spectral shapes with high-frequency falloff rates and corner frequencies through model fitting for the whole event and during the rupture. The combination of these two independent methods provides us a comprehensive and self-consistent set of observations, with independent phase and amplitude measurements. We apply our techniques to the M_w 8.3 2015 Illapel Earthquake, Chile (Figure 1). This earthquake resulted from the subduction of the Nazca Plate underneath the South American Plate with a convergence rate of ~70 mm/yr (https://earthquake.usgs.gov/earthquakes/eventpage/us20003k7a#region-info, last accessed 17 February 2017) and caused locally a tsunami wave as high as 11 m (Melgar et al., 2016). The fault dimension was probably 200 km × 200 km, and the maximum slip

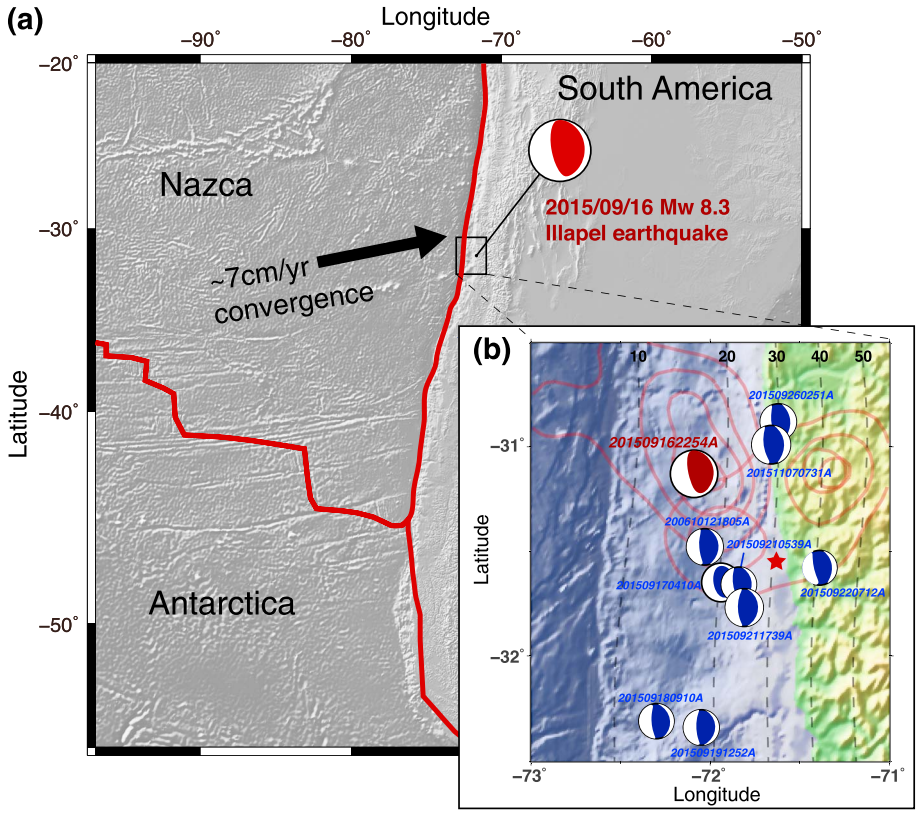

Figure 1. (a) Tectonic setting of southern Chile and location of the 2015 Illapel, Chile, M_w 8.3 earthquake. Red bold lines indicate the plate boundaries, and the black arrow shows the relative motion between the Nazca Plate and the South American Plate. The rectangle highlights the location of the insert and the earthquake source region. (b) Zoom-in of the source region: focal mechanisms (from GCMT) of the M_w 8.3 mainshock (red) and other $M_w > 6$ shocks (blue) selected as empirical Green's functions for this study. Red contours show the scaled backprojection energy distribution from Yin et al. (2016), which we use to represent the source region. The red star shows location of the M_w 8.3 epicenter. Black dashed lines indicate the plate interface depth from the slab 1.0 model (Hayes et al., 2012).

was found to be about 10 m by finite slip inversion of seismic data (e.g., Lee et al., 2016; Ye et al., 2015) and by joint inversion of seismic and tsunami waveforms (e.g., Heidarzadeh et al., 2015; Li et al., 2016). For this earthquake, Yin et al. (2016) used CS-BP of teleseismic *P* waves in two frequency bands and observed a clear dependence between frequency and locations of the energy bursts, which are interpreted as caused by stress change variations on the fault surface.

2. Improved Compressive Sensing Backprojection

The idea of Compressive Sensing (CS) for inverse problems was first proposed in the applied math and signal processing communities (Candès et al., 2006; Donoho, 2006) to allow sparsity of the models through minimization of the L_p norm with $0 < p \leq 1$. Yao et al. (2011, 2013) integrated this inversion technique with the backprojection method in order to study the seismic radiation of large subduction zone earthquakes ($M_w > 8$). Yin and Yao (2016) carefully tested and improved the CS-BP method to be less sensitive to potential data outliers, which may carry abnormal amplitudes or phases that affect the location of energy bursts. The sparsity constraint of the CS scheme increases the spatial resolution of seismic energy bursts during the rupture and provides an advantage to the conventional backprojection (Ishii et al., 2005) as well as to beamforming methods (Yin & Yao, 2016).

Our CS-BP method uses a sliding time windows technique (Yao et al., 2011; Yin & Yao, 2016). We first preprocess the *P* wave velocity seismogram at each station of a seismic array (see Yin & Yao, 2016, or supporting information Figure S1 for details; VanDecar & Crosson, 1990). Then for each sliding time window, we take

the Fourier transform and construct a data spectra vector $\mathbf{b}(f)$ that depends on frequency with a dimension of the number of stations N. Our source model is a complex vector $\mathbf{x}(f)$, which is projected on a flat plane at the hypocenter depth and contains seismic amplitudes from potential sources located at M grid points generating the pulse in that particular P wave window. Moreover, we mitigate the local site effects by normalizing the seismograms. The reference time t_{n0} is the travel time from the hypocenter to the station n,and the travel time between the location of each grid point m to each station n is τ_{nm}. The theoretical global P wave arrival times are based on the IASP91 velocity model (Kennett & Engdahl, 1991). Wave propagation is simplified to a time shift in the frequency domain, and we construct the propagation matrix $\mathbf{A}(f)$ of size $N \times M$ with entries:

$$A_{nm}(f) = e^{-2i\pi f(\tau_{nm} - t_{n0})}. \tag{1}$$

The basic idea of CS is to invert the system $\mathbf{b}(f) = \mathbf{A}(f)\mathbf{x}(f)$ for the sparse source vector $\mathbf{x}(f)$ by minimizing the misfit function

$$\phi(\mathbf{x}) = \|\mathbf{A}(f)\mathbf{x}(f) - \mathbf{b}(f)\|_1 + \lambda\|\mathbf{x}(f)\|_1, \tag{2}$$

where λ is a damping factor that attunes data misfit (first term in equation (2)) and model L_1-norm constraint (second term in equation (2)). A balance between the residual and model norms in this problem guides us to find a proper damping factor $\lambda = 0.6 \times N$ that corresponds to both well-fitted data and acceptable model sparsity. We refer to Yao et al. (2011) and Yin and Yao (2016) for more discussion on the choice of λ. We solve the sparse inversion problem using the CVX package (http://cvxr.com, last accessed 3 November 2012) based on convex optimization and the interior point method (Boyd & Vandenberghe, 2004). Two important specificities of our method affect the inversion: (1) the meshing of the model $\mathbf{x}(f)$ and (2) the truncation of the time window on the spectra data $\mathbf{b}(f)$. This study focuses on these two factors to improve the conventional CS-BP.

2.1. Autoadaptive Refinement of the Source Grid

In our CS problem, the number of model parameters in $\mathbf{x}(f)$ equals the number of grid points in the source region. One might want to densify the source region, that is, increase the number of grid points, to improve the data fitting and enhance the spatial accuracy of sources. However, a uniform and denser mesh of the source region (or in the model space) will greatly decrease the numerical efficiency of the inversion due to the larger dimension of the inversion (equation (2)) and unnecessary computation spent on the points with zero amplitude in our sparse description. Therefore, we develop an autoadaptive grid refinement scheme to improve both numerical efficiency and spatial resolution of our method.

We use a synthetic test to construct the iterative grid refinement scheme. The synthetic model is simplified to a two-spike source model with 10% random noise added to the data $\mathbf{b}(f)$ at a frequency $f = 0.5$ Hz (Figure 2). We first start with a uniform and coarse mesh (40 km spaced grid points) on a 360 km × 320 km source region, that is, totally $9 \times 8 = 72$ unknown model parameters. After first inversion, we select only a few grid points that have amplitudes exceeding 10^{-6} times the maximum amplitude of all grid points (Figure 2b). Then, we refine the mesh by a factor of 2 in the region with those selected grid points and perform the inversion again. We repeat these steps until a grid size of 5 km × 5 km. If we uniformly mesh the source region with a grid size of 5 km, we need to solve a total of 4,745 unknown model parameters, most of them being null in the sparse representation. However, with the autoadaptive gridding method, we only need to solve the equations four times with about 100 model parameters at each step. With the unnecessary and redundant computation discarded, we can get the robust CS-BP results in both high spatial resolution as well as in good computational efficiency while remaining within reasonable physical constraints. The computational runtimes for this test case are shown in the supporting information (Figure S2).

2.2. Reference Source Adjustment Technique

The key idea of backprojection methods is to correctly align the seismograms to obtain the constructive and destructive interferences (Ishii et al., 2007). For the time domain methods, these locations can be backprojected by aligning and stacking waveforms based on the travel time from each grid point in the source region to each receiver. For frequency domain methods, the alignment is first performed at the beginning part of the direct P waves, according to the hypocenter and to the individual phase shifts within of each station (Meng et al., 2011; Yao et al., 2011). Attempts to improve the temporal and spatial resolution have been made through accurate time correcting/phase shifting, enhancement of the signal coherency, or mitigation of stacking artifact. For instance, elaborate alignment and stacking techniques have been proposed and

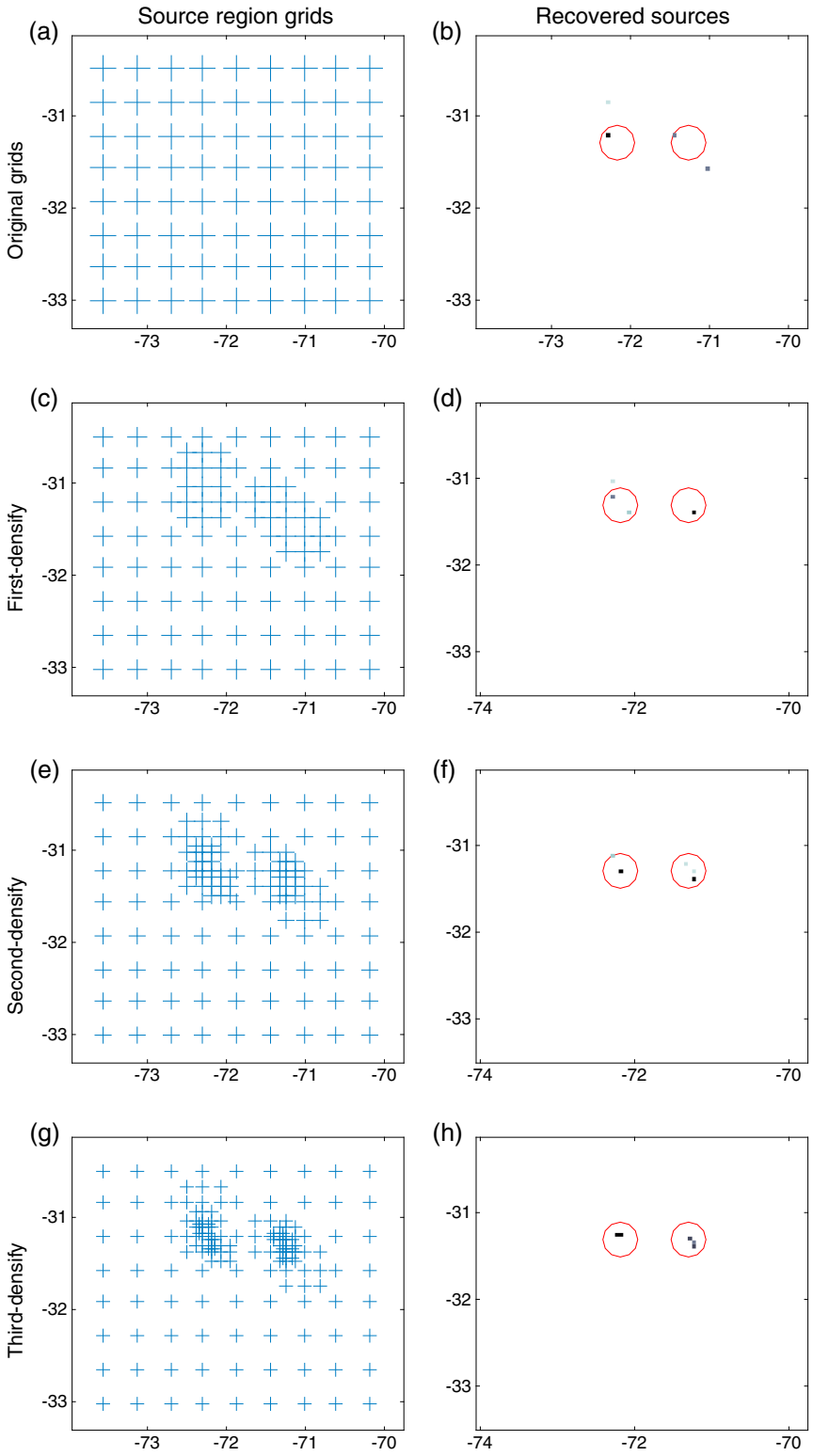

Figure 2. Synthetic test from the autoadaptive source grid refinement scheme. (a, c, e, and g) The blue crosses show the grid points used in the inversion. (b, d, f, and h) The dots show the results recovered from the corresponding grids, and the red circles indicate the positions of our synthetic sources (circle centers).

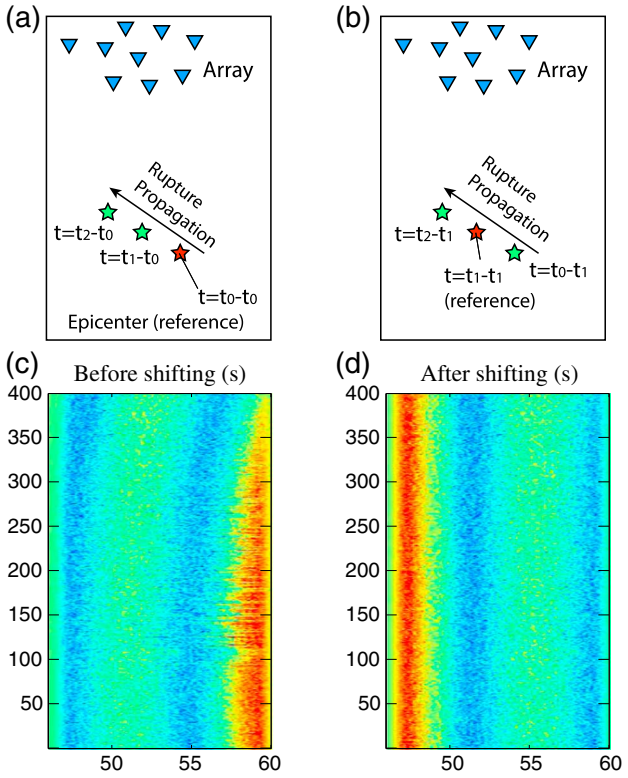

Figure 3. (a, b) Schematic illustration of the reference source adjustment technique and one example of waveform "truncation effect" (c) before and (d) after reference source adjustment.

tested by Xu et al. (2009). Meng et al. (2012) suggest a strategy for the reference window to mitigate the "swimming artifact" due to nonstationary signals as well as the array geometry; and in conventional CS-BP better source times are achieved by correcting the time difference between the sliding window time and source time (Yao et al., 2011; Yin & Yao, 2016).

Specifically for the conventional CS-BP technique (Yao et al., 2011; Yin & Yao, 2016), the reference location of waveform alignment remains unchanged at the hypocenter and for all the sliding time windows. However, for large earthquakes ($M_W > 8$), as the rupture propagates, the later *P* waves originating from different source locations rather than the fixed reference point (e.g., the hypocenter) can bias the alignment in each individual sliding time window. This introduces an apparent time shift that typically grows with rupture distance and that results in a loss of coherency in the truncated time window in the later rupture period. Figure 3c illustrates this effect and shows that it leads to a partial sampling (truncation) of the coherent signal in the later time windows. It is more pronounced in the low-frequency waveforms, where the period approaches that of the length of the sliding window, and we refer to this issue as the "truncation effect." It may bring systematical bias to the data vector $\mathbf{b}(f)$ and blurring artifacts of the recovered sources (Figure 4b).

Instead of solely aligning the entire waveforms to direct wave travel time from the fixed hypocenter (Figure 3a), we propose a Reference Source Adjustment Technique (RSAT). The first window is aligned based on travel times between the hypocenter and the receivers. For later windows, we solve for the position of the highest radiated energy burst *r*, calculate the new relative travel time shift t_{nr} between the new reference location and station *n*, and use it to realign the waveforms in the current time window (Figure 3d). This procedure leads to the new data vector $\mathbf{b}'(f)$ and updates the phase spectrum matrix $\mathbf{A}'(f)$, whose values are

$$A'_{nm}(f) = e^{-2i\pi f(\tau_{nm} - t_{nr})}. \quad (3)$$

The new system of equations becomes $\mathbf{b}'(f) = \mathbf{A}'(f)\mathbf{x}(f)$, and the procedure is repeated when sliding through the entire waveforms. The waveform truncation effect can be greatly suppressed as illustrated in Figure 3. Since we only have one reference position for each time window, this technique is most efficient for generally unilateral ruptures.

In this section, we construct synthetic time series to verify the improvements of our technique. We set 4 point sources, each separated in space by 42 km and in time by 20 s, to mimic a northwestward unilateral rupture with a propagation speed of 2.1 km/s. The synthetic source plane is set at the depth of 20 km to represent the hypocenter depth of the 2015 Illapel Earthquake, and the 400 synthetic receivers are at the location of the USArray stations. Similar to our previous work (Yin et al., 2016; Yin & Yao, 2016), we extract and taper the first 12 s of the M_w 8.3 mainshock seismograms recorded by each station and use these wavelets as synthetic waveform. We compute the travel time using the IASP91 velocity model, insert the wavelets to their corresponding arrival times, and add random noise (in time domain, with amplitudes lower than 10% of the peak signal amplitude). Figure 4a shows that the waveforms are aligned with respect to the hypocenter location and the later phases (around 40 s and 60 s) are subject to the shift due to the northwestern rupture propagation. We solve for equation (2) using $\mathbf{A}(f)$ of equation (1) (without RSAT, Figures 4b and 4d) and $\mathbf{A}'(f)$ of equation (3) (with RSAT, Figures 4c and 4e). We find that without RSAT, while the overall pattern of rupture propagation can be recovered (Figure 4b), there are many artifacts in between the synthetic point sources (Figures 4b and 4d) that blur the location of the sources. In contrast, the RSAT is able to better recover each point source (Figures 4c and 4e), with limited blurring artifacts in between. A relatively more elaborate synthetic test can be found in Figure S3 of the supporting information.

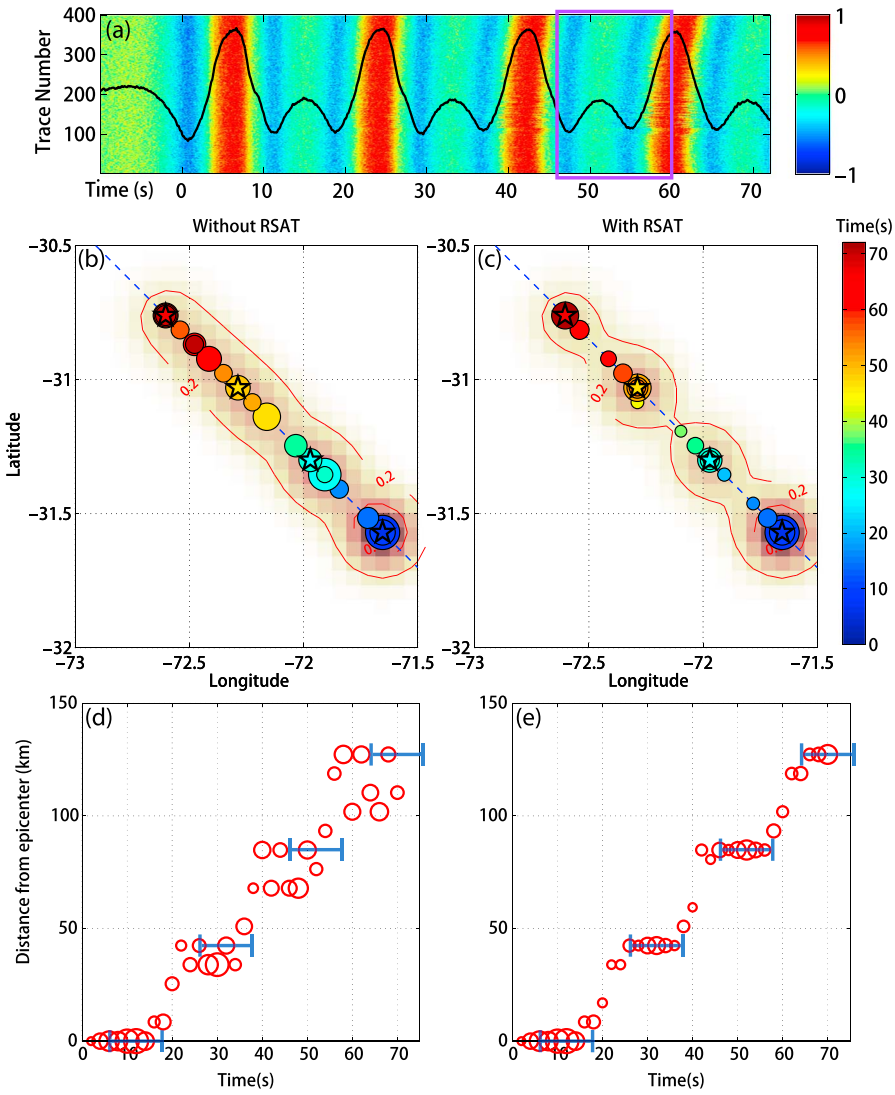

Figure 4. Synthetic test for the reference source adjustment technique (RSAT). Top panels: (a) synthetic time domain waveforms recorded at each station where the color scale indicates the waveforms amplitude, the centered black waveform is the stacked seismogram, and the purple box shows the waveform within 40–60 s (similar to the waveform in Figure 3). Middle panels: results from (b) conventional and (c) improved CS-BP method where the stars represent our synthetic sources, the circles are the recovered sources colored by source (or rupture) time, the background copper color scale corresponds to the total energy, the red contours indicate 20% of the energy maxima, and the dashed lines show the synthetic rupture direction. Bottom panels: location of the energy bursts against time from our synthetic source (blue segments) and recovered from (d) conventional and (e) improved CS-BP (red circles, left and right, respectively).

By combining both the autoadaptive source grid refinement method and the reference source adjustment technique, our improved CS-BP, ImCS-BP, is able to provide more accurate positions of radiated energy bursts, which should help to constrain the spatiotemporal evolution of the dynamics of large earthquakes.

2.3. Data for the ImCS-BP

We apply our ImCS-BP method to the teleseismic *P* wave velocity seismograms of the 2015 M_w 8.3 Illapel Earthquake recorded by the USArray stations in North America (TA array, data available using Wibler 3 of the Incorporated Research Institutions for Seismology Data Management Center, IRIS-DMC, http://ds.iris.edu/wilber3/find_event). Details of the data processing can be found in the supporting information (Figure S1), and in Yin et al. (2016). Here we emphasize the adaptive meshing scheme and reference source adjustment improvements. We choose to solve for a potential source region of dimensions 432 km × 432 km.

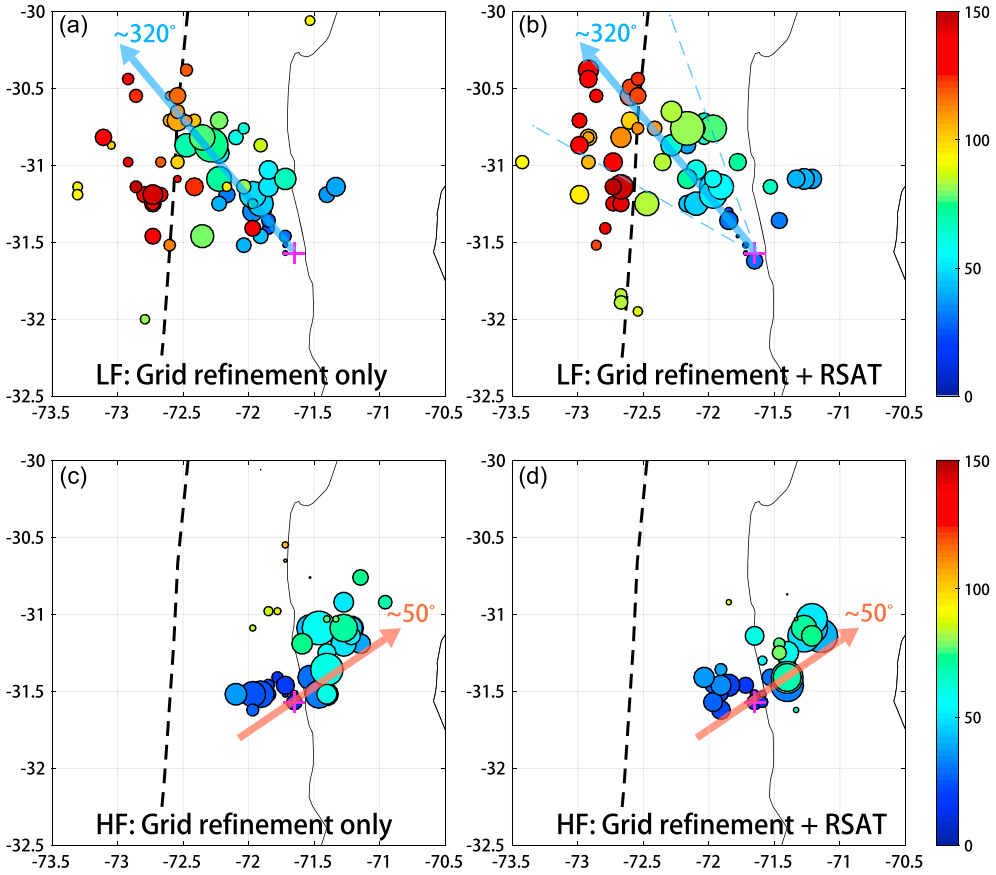

Figure 5. Comparison of CS-BP with ImCS-BP results of the 2015 M_w 8.3 Illapel Earthquake. The black dashed lines show the trench. The arrows represent the assumed direction of propagation of the energy bursts. The solid circles indicate the energy bursts, their colors correspond to the time of the burst since the onset of the earthquake, and their size corresponds to the amplitude power of energy bursts ($|\mathbf{x}(f)|^2$). Low frequency (0.08–0.5 Hz) results (a) without and (b) with RSAT. The azimuths 300° and 340° drawn in blue thin dashed lines are used to estimate a propagation velocity in Figure 6a. High frequency (0.5–1 Hz) results (c) without and (d) with RSAT.

To apply the autoadaptive source grid refinement, we set a preliminary grid size of 48 km × 48 km (9 × 9 = 81 grid points) and iteratively refine until reaching a grid size of 6 km × 6 km. The choice of the sliding time window length can be bounded. The lower bound should be at least greater than the longest period resolvable in the respective frequency bands (i.e., 1/0.08 Hz = 12 s, and 1/0.5 Hz = 2 s). The upper bound of the time window length is generally empirical (by trial) and should be considered carefully. A long time window may include too many subevents (radiators) in each window, weakens the coherency, and reduces our ability to resolve small radiators. Here we choose window length of 14 s for the 0.08–0.5 Hz low-frequency (LF) band and of 8 s for the 0.5–1 Hz high-frequency (HF) band. RSAT is applied for each time window to suppress the waveform truncation effect.

2.4. Evolution of the Seismic Energy Bursts

Our ImCS-BP method provides the spatial and temporal evolution of the seismic energy bursts during the rupture of the Illapel Earthquake. We show the results with (1) autoadaptive grid only (Figures 5a and 5c) and (2) autoadaptive grid and RSAT (Figures 5b and 5d). While the overall patterns of the seismic energy distribution are similar in both cases, the results with RSAT (Figures 5b and 5d) are less scattered, which we attribute to appropriate suppression of the truncation effect. The most obvious improvement of RSAT appears in the later part of the rupture (from 80 s to 150 s) in the low-frequency band (Figures 5a and 5b). This is expected as the waveform truncation effect is more severe for the late stage using low-frequency data (see supporting information Figures S1 and S4).

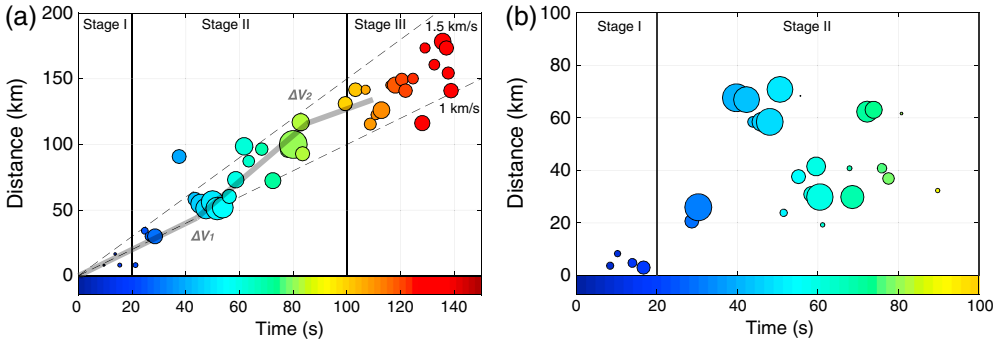

Figure 6. Distance (*y* axis) of energy bursts against time (*x* axis) for (a) LF (Figure 5b) and (b) HF (Figure 5d). We select the energy bursts between 300° and 340°, project on the axis defined from the epicenter to an azimuth of 320° (see arrow in Figure 5), and estimate the range between bursts and epicenter (Figure 6a). We select all bursts for HF results and show their distance from the epicenter (Figure 6b). The circles are sized proportionally to the amplitude of energy bursts, colored with time using the same scheme as in Figure 5.

Given the evolution of energy bursts with time, we refer to stage I as the first 20 s of the rupture, stage II as the rupture time between 20 s and 100 s, and as stage III the time beyond that. The source locations of the low-frequency (LF, 0.08–0.5 Hz) and the high-frequency (HF, 0.5–1 Hz) bands appear to express different behaviors of the rupture (Figure 5).

Most of the LF energy (Figures 5a and 5b) propagates unilaterally from the epicenter to a northwest direction (toward the trench) during stages I and II. Weak LF energy bursts also radiate in the northeast direction from the epicenter (stage I). In stage III, the LF energetic bursts are located well beyond the trench in the outer-rise region, which we attribute to the water reverberations and provide more detailed discussion in section 4.1. In contrast, the HF bursts first propagate from the epicenter to the west for about 20 s (stage I) and then come to a pause. From 30 s to 70 s (early stage II), secondary HF pulses propagate to the downdip part of the megathrust, about 90 km northeast of the epicenter (Figures 5c and 5d). Inspecting the evolution of these two frequency bands may present a quite different signature of the evolution of the source: the LF radiation migrates updip (azimuth ~320°, Figures 5a and 5b), while the HF radiation migrates downdip (azimuth ~50°, Figures 5c and 5d). Results from both frequency bands suggest no southward rupture propagation.

If the migration of the energy bursts represents the propagation of the rupture front, the LF ImCS-BP results can also provide a rupture velocity estimate. Most of the energy bursts are within the azimuth range 300°–340°, and we calculate a propagation speed from the time-distance plot shown in Figure 6a. The average propagation speed is around 1.0–1.5 km/s, which is much slower than a globally averaged shear wave speed of 3.75 km/s at the centroid depth (IASP91 model, Kennett & Engdahl, 1991). As for the HF energy bursts (Figure 6b), they are generally clustered along a 50° azimuth, but no estimate of propagation speed seems reliable.

3. Spectral Source Analysis

Our ImCS-BP method can provide relevant observational information about the location and timing of high-frequency bursts. However, the location of the radiated bursts found by ImCS-BP shows mostly *P* waveform coherency. In order to provide additional observational constraints on the rupture dynamics of the Illapel Earthquake, we complement our backprojection analysis with a spectral analysis method that was initiated in Denolle et al. (2015) and in Denolle and Shearer (2016).

3.1. Data for the Source Spectral Analysis

We choose nine events of magnitude $M_w > 6$ that occurred nearby the mainshock (Figures 1b and Table 1). We download teleseismic *P* wave displacement data recorded at all stations located with 30° and 90° of angular distance and that are available from the Federal Digital Seismographs Network (FDSN) (see a map of their location in supporting information Figure S5) using Obspy (see Beyreuther et al., 2010, also available at

Table 1
Source Information of the Selected M_w 6 Earthquakes (the eGf 1Events)

Event (GCMT ID)	Moment magnitude	Seismic moment (10^{18} Nm)	Number of stations	Centroid depth (km)	Corrected depth (km)	Corner frequency (Hz)	Falloff rate	Madariaga stress drop (MPa)
200610121805A	6.4	4.28	92	36.8	32.8	0.33	2.8	31.8
201509170410A	6.8	17.4	117	36	38	0.13	2.2	7.4
201509180910A	6.1	1.77	124	15	27	0.33	2.8	13.1
201509191252A	6.2	2.67	236	20	34	0.33	2.8	19.8
201509210539A	6.1	1.78	243	37	33	0.45	3.0	34.3
201509211739A	6.6	9.62	297	39	45	0.33	3.0	50.2
201509220712A	6.1	1.51	215	50	72	0.62	3.2	53.0
201509260251A	6.3	3.21	286	46	58	0.45	3.0	43.4
201511070731A	6.7	14.8	201	43.4	55.4	0.33	3.0	77.2

Note. Gray-shading rows indicate the events without overlaying water layer.

https://github.com/obspy/obspy/wiki). The preprocessing of the data consists in removing means, trends, instrumental responses, and integrating to displacement waveforms. We cut 300 s long waveform windows for the Illapel Earthquake, starting 15 s before and ending 285 s after theoretical direct *P* wave arrival time (calculated by IASP91 model, Kennett & Engdahl, 1991), and we use a magnitude-dependent window length for the small shocks to capture mostly their source time function ($T_d \sim 10^{(M_w-3.3)/2}$, e.g., 30 s for M_w 6.1–6.3; 40 s for M_w 6.4–6.6; and 50 s for M_w 6.7–6.8). We apply a Tukey window that tapered 10 s on either end of the window so the total window length is (T_d + 20) s.

In order to only select high-quality data, we first perform visual inspection, then calculate a signal-to-noise ratio (SNR), and finally decide on a SNR threshold. Our noise estimate is taken in the window before the *P* arrival (using the same window length as that of the signal), we then Fourier transform both signal and noise windows, and define the SNR as the log of the ratio between the mean amplitude of the data and the noise in two frequency bands (0.02–0.5 Hz and 0.5–2 Hz). We select stations where the SNR exceeds 2 dB in both frequency bands (supporting information Figure S6). The remaining data consist in a total of 1,811 waveforms that provide a relatively good azimuthal coverage given the location of the mainshock (Southern Hemisphere) with respect to the distributions of global seismic stations (see map in supporting information Figure S5).

3.2. Removing Path Effects

The relation between the far-field *P* wave vertical displacement waveform $u^n(t)$ recorded at station *n* and the moment-rate function $s(t)$ can be written as follows:

$$u^n(t) = s(t) \otimes g^n(t), \tag{4}$$

where $\otimes$ denotes convolution in the time domain and $g^n(t)$ is a far-field elastodynamic Green's function (or spatial derivatives of the displacement Green's function if the source is a double couple) from the source to the *n*th station that comprises the wave propagation along the raypath. Transforming equation (4) into the frequency domain, we obtain the far-field *P* wave displacement as

$$U^n(f) = S(f)G^n(f), \tag{5}$$

where $U^n(f)$, $S(f)$, and $G^n(f)$ are the amplitudes of the Fourier transforms of the displacement seismogram, source moment-rate function, and Green's function, respectively. To recover the earthquake source term $S(f)$ from the observed seismogram spectrum $U^n(f)$, it is essential to properly remove the effects from the wave propagation, that is, the Green's function term $G^n(f)$. We use a two-step strategy to remove path effects that was proposed in Denolle and Shearer (2016) and that combines theoretical simple Green's functions with empirical Green's functions (eGfs).

The principle of the eGf approach is to use small events nearby the large earthquake to calibrate for the true 3-D path effects, provided that we can construct their own source term. We do so by removing their path terms from a simplified and theoretical Green's function. The small earthquakes should share the same raypaths (i.e., Green's function) and the same focal mechanism (i.e., radiation pattern) as the large event. Without knowing the source spectrum of the small events, we are left with performing a spectral ratio (e.g., Asano &

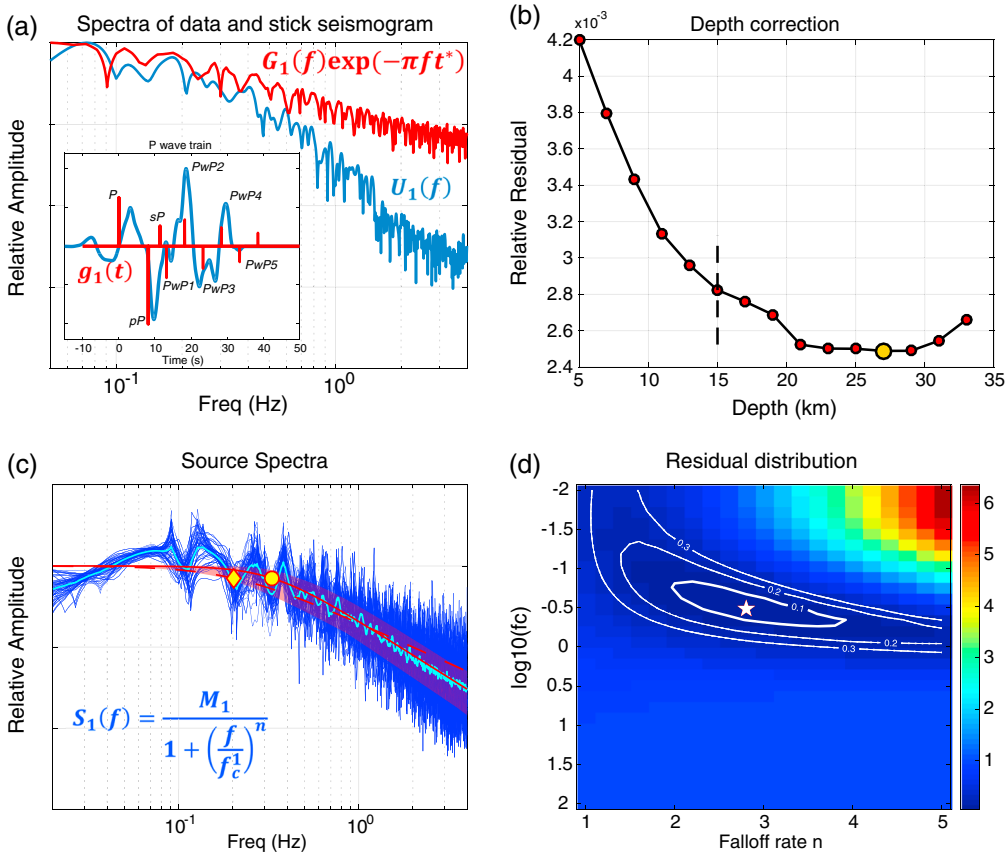

Figure 7. Steps to retrieve the source spectra for the small events, using the 18 September 2015 M_w 6.1 event as example. (a) (red line) Spectra of a synthetic Green's function with global attenuation model from Warren and Shearer (2000) and (blue line) the data recorded at station AZ.FRD. With the corrected source depth, the synthetic Green's function $g_1(t)$ with *P* wave train (stick seismogram in the inner panel, compared with the recorded *P* waveform) can be constructed and used to estimate a source spectrum. (b) Search of the source depth for the small event by fitting the spectral shape in Figure 7a. The dashed line indicates the GCMT centroid depth, and the yellow circle shows the best fit source depth. (c) The (cyan) spectrum is stacked over individual stations (blue spectra) and fit to a single-corner frequency model (red solid curves, equation (7)), with the corner frequency indicated by the yellow circle and an equivalent model with a stress drop of 3 MPa and falloff rate of 2 (dash red line and yellow diamond marker). The red shadow region indicates the uncertainty from the model fitting, which is constructed by model parameters within the 0.1 residual contours in Figure 7d. (d) Misfit distribution of the spectra fitting for the two parameters. Contours indicate the fitting residual levels of 0.1, 0.2, and 0.3. The white star indicates the minima of fitting residual as well as the corresponding corner frequency f_c and falloff rate *n*.

Iwata, 2012; Miyake et al., 2003). However, it has limited value when trying to explore the high-frequency falloff rates as it only provides the relative falloff rate between the large and small events. One alternate strategy is to apply a theoretical model with global average parameters such as taking a uniform static stress drop of 3 MPa on a circular crack, a high-frequency falloff rate of 2, and a single-corner frequency parametric model such as that in Aki (1967), Brune (1970), and Baltay et al. (2014). In the eGf method, the source spectra of both small and large events are tightly related since the falloff of the small event spectra directly controls the falloff of the large event spectrum. If the eGf quake is small enough (common practice is to use 2–3 magnitudes lower than the target event magnitude), the potential bias would be reduced. With teleseismic data, it is difficult to retrieve data with high SNR for low-magnitude events. Solving for the small quake source spectrum is thus an attempt to reduce this effect. Our spectral analysis method is summarized in Figure 7.

3.2.1. Getting the Path Effects From Small Events (M_w ~ 6)

The first step is to obtain the source spectra of the small events. The *P* wave train of shallow earthquakes contains not only the direct *P* but also the *P* wave reflections to the free surface (pP and sP) that greatly bias the displacement spectra (Denolle et al., 2015; Denolle & Shearer, 2016; Houston & Kanamori, 1986; Warren &

Shearer, 2005). In addition to the free surface effects, the direct *P* waves of shallow offshore earthquakes reverberate in the water column, potentially also interfering with the *P* wave train and altering their spectral shapes. In this study, we apply both the depth-phase approach of Denolle et al. (2015), Denolle and Shearer (2016), and the water-phase filter proposed by Akuhara and Mochizuki (2015) to correct our *P* wave train displacement spectra. We solve for the free surface reflections and water phases in a fluid-over-elastic half-space medium, ignoring the accretionary wedge structure above the source that likely contains low-velocity sediments and high attenuation (Yue et al., 2017). We regard the small events as point sources and directly calculate their response $g_1(t)$ and where $G_1(f)$ is the corresponding amplitude spectrum. Effectively, $g_1(t)$ is a stick seismogram constructed to represent the (attenuation free) Green's function convolved with the moment tensor of the point source and with a delta pulse as a source time function:

$$g_1(t) = A_P\delta(t) + A_{pP}\hat{R}_P\delta(t - t_{pP}) + A_{sP}\hat{R}_s\delta(t - t_{sP}) + \sum_{l=1}^{\infty} A_l(-1)^l\acute{T}\hat{r}^{l-1}\grave{T}\delta(t - t_l). \quad (6)$$

The right-hand side terms of this equation represent the direct P, pP, sP, and water phases with arrival time of $t_P = 0$ (waveforms are aligned to the direct P), t_{pP}, t_{sP}, and t_l, respectively. $\hat{R}_P$, $\hat{R}_s$ are respectively the *P* and *S* wave reflection coefficients at the water-solid interface. $\acute{T}$ and $\grave{T}$ are transmission coefficients of the upgoing and downgoing *P* wave at the water-solid interface. $\hat{r}$ is the reflection coefficient at the water-air interface. A_P, A_{pP}, A_{sP}, and A_l are the amplitude terms that contain geometrical spreading $1/4\pi\rho c^3R$ (c seismic wave speed, R source-receiver raypath length) and radiation pattern. l is the order of water phases, that is, the number of times the *P* wave reverberates in the water column, taken high enough (20 or 30) to retrieve the phases within the time window. Finally, the Earth attenuation is imposed in frequency domain using a global t^* attenuation modeled as $G_1(f)\exp(-\pi ft^*)$ (Warren & Shearer, 2000; Figure 7a). The source depth controls the relative arrival times (phase) and the radiation pattern terms (amplitude) of the *P* wave train, which gives low-frequency asymptote and harmonic troughs in the Fourier amplitude spectrum. We thus attempt to constrain the source depth that best fits the Fourier amplitude spectrum between data and synthetics. For $M_w \sim 6.5$ earthquakes, we multiply the attenuated Green's function with a normalized source spectrum $S(f) = \frac{1}{1+(f/0.1)^2}$ with corner frequency 0.1 Hz chosen based on global observations (Allmann & Shearer, 2009; Denolle & Shearer, 2016) and then obtain the optimal depth that minimizes the difference between the synthetic and the observed spectra (Denolle et al., 2015; Denolle & Shearer, 2016; Warren & Shearer, 2005; Figure 7b). The corrected source depths, found to be mostly consistent with the GCMT (Global Centroid Moment Tensor Catalog, http://www.globalcmt.org) centroid depths, are listed in Table 1.

Ignoring directivity effects in the small events, we can recover a single reliable far-field *P* wave source spectrum for each small event by deconvolving (division in the frequency domain) the observed *P* wave train displacement spectra with $g_1(t)$ (source depth corrected) and stack over all stations. We fit the source spectrum to a single-corner frequency model,

$$S_1(f) = \frac{M_1}{1 + \left(\frac{f}{f_c^1}\right)^n}, \quad (7)$$

where M_1 is the seismic moment of each small earthquake (GCMT catalog, Table 1; Ekström et al., 2012), f_c^1 is the corner frequency, and n is the high-frequency falloff rate. Because the corner frequency of those events is within our frequency band, we can normalize the source spectra $S_1(f)$ to the corresponding seismic moment. Figure 8 shows the source models of all the eGf events.

To find the two source parameters (corner frequency and high-frequency falloff rate) of equation (7), we minimize the L_2-norm misfit in log space between the shapes of measured and modeled spectra. We proceed with a grid search and show that the shape of the misfit function highlights a correlation between the two parameters (Figure 7d and supporting information S1). To account for the uncertainty derived from this parameter trade-off, we take all the models within the misfit contour of 0.1 and use the region illustrated by these models as the uncertainty of the eGf spectral model (Figures 7c and 7d, also see supporting information S1). In addition to this correlation, the high-frequency falloff rate directly trades off with our choice of attenuation. We also implemented a spatially variable attenuation model (Warren & Shearer, 2002) but found no difference in the corner frequencies and only a slightly larger falloff rates in our estimates (see supporting

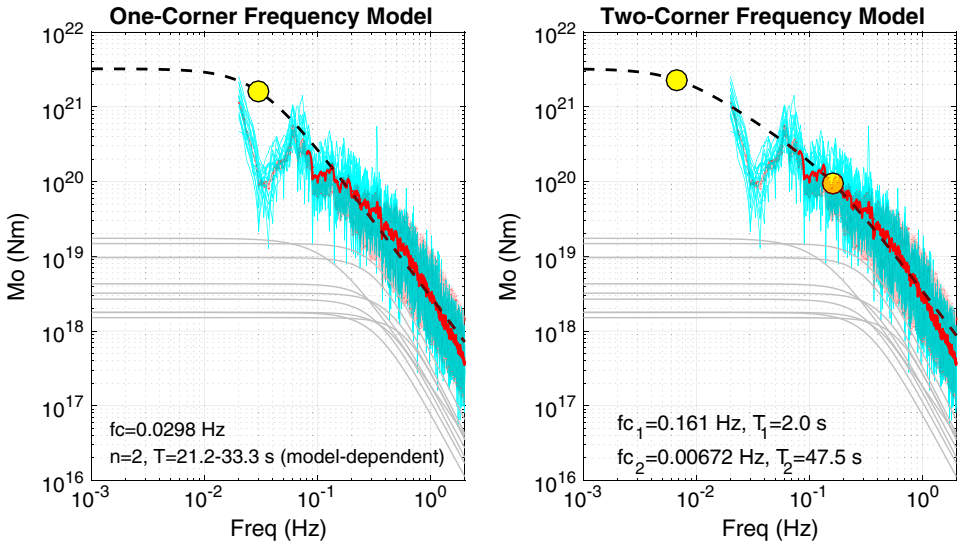

Figure 8. Source spectrum fitting for the M_w 8.3 Illapel Earthquake. Fitting with (left) a single-corner frequency model and (right) a double-corner frequency model. Cyan lines are the source spectra measured and averaged in each azimuth bin of 10°. Red lines are the stacked source spectra measurement in 0.08 Hz–2 Hz, bandwidth that is used to fit with the spectral source models. Red shadow region shows the uncertainty of the main event source spectrum, which is propagated from the uncertainty of eGf source spectra. Gray thin lines are the best fit source spectral models of the small events. Black dashed lines indicate the best fitted model with yellow circles to show their corner frequencies. Optimal source parameters (corner frequency, their associated duration, and high-frequency falloff rates) are also shown in the bottom of the panels.

information Table S1). For simplicity, we use the globally averaged t^* model (Warren & Shearer, 2000). Interpretations on the small event source parameters are not the focus of this study. However, we validate that our results are reasonable through estimates of static stress drop, assuming a simple circular crack model with uniform stress drop,

$$\Delta\sigma = \frac{7}{16}\left(\frac{f_c}{k\beta}\right)^3 M_1, \tag{8}$$

where β is the S wave velocity and $k = 0.32$ (Eshelby, 1957; Madariaga, 1976). We find that the values of stress drop (Table 1) are comparable to the global averages (Allmann & Shearer, 2009; Denolle & Shearer, 2016). With the best fit parameters, we use the spectral model of the small events (equation (7)) to recover the spectra of the large event.

3.2.2. Source Spectrum of the Main Event

The eGf method relies on the common Green's function $G(f)$ between two earthquakes of interest. Given $U_2(f)$ the observed P wave train displacement spectrum of the large shock, and $U_1(f)$ that of the small shock (Figure 5c):

$$U_1(f) = S_1(f)G(f), \tag{9}$$

$$U_2(f) = S_2(f)G(f), \tag{10}$$

with $S_2(f)$ is the target source spectrum, $S_1(f)$ is the small even source spectrum (found in the first step). We combine equations (9) and (10) and find that

$$S_2(f) = \frac{U_2(f)}{U_1(f)} S_1(f). \tag{11}$$

We stack all the source spectra for all small (eGf) events at all stations by averaging the log of the amplitudes and weighting by the number of stations within each 10° azimuth bin. In addition, based on equation (11), the uncertainties in the eGf spectra $S_1(f)$ can be propagated to the target source spectrum. Figure 8 shows a stable source spectrum with uncertainty of the Illapel Earthquake.

We can calculate the *P* wave radiated energy by integrating the squared velocity spectrum within a frequency band [f_1 f_2] assuming a homogeneous, isotropic, and elastic medium around the source:

$$E_P = \frac{8\pi}{15\rho\alpha^5}\int_{f_1}^{f_2}|fS_2(f)|^2 \mathrm{d}f, \tag{12}$$

in which ρ = 2.92 g/cm^3 is the density from the PREM model (Preliminary Reference Earth Model, Dziewonski & Anderson, 1981) and α = 6.5 km/s is the *P* wave velocity from IASP91 model (Kennett & Engdahl, 1991). If we assume that both *P* and *S* waves share the same spectral shape, then the ratio of S-to-P radiated energy is $3\alpha^5/2\beta^5$ and the total radiated energy becomes

$$E_{\text{total}} = \left(1 + 3\alpha^5/2\beta^5\right)E_P. \tag{13}$$

We use β = 3.75 km/s, the shear wave speed from IASP91 model at the centroid depth. The total radiated energy must be estimated by integrating over the frequency interval [0 ∞] Hz. However, we have a limited frequency band within [0.02 2] Hz. We can use a parametric description of the source model to estimate the proportion of radiated energy missing from our limited frequency band. We estimate the radiated energy at each azimuth bin and average these estimates weighted by the number of stations in each azimuth bin.

3.3. Total Event Source Spectrum

Table 1 summarizes the best fit source depths and parameters necessary to construct $S_1(f)$ for each eGf. We use these source models of small events (shown in Figure 8) to apply the eGf method and retrieve the M_w 8.3 mainshock source spectrum $S_2(f)$.

Despite the differences in the small events source models (Figure 8), the recovered mainshock source spectra all share a similar shape at various azimuths (Figure S7). Because the corner frequency of large earthquakes ($M_w > 8$) is lower than the low-frequency cutoff of our data, we only recover part of the source spectrum and cannot normalize the spectrum to the seismic moment (Figures 8 and S7). However, unlike the case of the small events, $S_2(f)$ has the absolute level of amplitudes, that is, it is scaled to the true seismic moment of the mainshock through the eGf approach. Furthermore, we can use the independently estimate of seismic moment (GCMT catalog) as an additional constraint to calibrate the amplitude level of spectra at $f \rightarrow 0$ Hz (Denolle & Shearer, 2016).

At all azimuths, the recovered source spectra of the M_w 8.3 event carry an unusual pattern at low frequencies 0.02–0.08 Hz. They are characterized by a steep drop in amplitude at 0.03–0.04 Hz (~20–30 s), indicating a loss of low-frequency energy (equation (12)), which we will address in section 4. At frequencies greater than 0.08 Hz, we test two parametric source models to fit the spectral shape.

The first model is the same as equation (7) with the seismic moment M_0 of the main event. It is a "classic" single-corner frequency model (Aki, 1967; Brune, 1970) with variable falloff rate *n*. We find that the best fit corner frequency from this single-corner frequency model is high, about 0.03 Hz (duration *T* varies from $2/\pi f_c$ = 21.2 s to $1/f_c$ = 33.3 s; Hanks, 1979) and a falloff rate *n* of 2. The second model is a double-corner frequency model inspired by the Haskell source model (Haskell, 1964) proposed by Denolle and Shearer (2016):

$$S_2^{\text{rec2}}(f) = \frac{M_0}{\sqrt{\left[1 + \left(\frac{f}{f_{c1}}\right)^2\right]\left[1 + \left(\frac{f}{f_{c2}}\right)^2\right]}}. \tag{14}$$

The two corner frequencies, which may correspond to source duration and to risetime, are 0.0067 Hz (duration $T_2 \sim 1/\pi\ f_{c2}$ = 47.5 s) and 0.16 Hz (duration $T_1 \sim 1/\pi\ f_{c1}$ = 2.0 s). The event durations estimated from the corner frequency models (equations (7) and (14)) likely underpredict the true event duration but may correspond to duration of the highest moment release that we find to be between 20 s and 70 s. We also show the spectra averaged over all eGfs and stations at each azimuth bin, their best fit models and source parameters in supporting information Figure S7, and summarize the azimuthal variations of the source parameters in Figure S8. Finally, by integrating the stacked spectrum (red spectrum in Figure 8) using equations (12) and (13), we find the total band-limited radiated energy of the M_w 8.3 earthquake to be 1.10×10^{17} J within 0.08 Hz–2 Hz (and 1.06×10^{17} J within shorter band of 0.08 Hz–1 Hz, for further comparison in the next section). Taking the uncertainties of source spectrum (shown by red shadow in Figure 8), the total band-limited

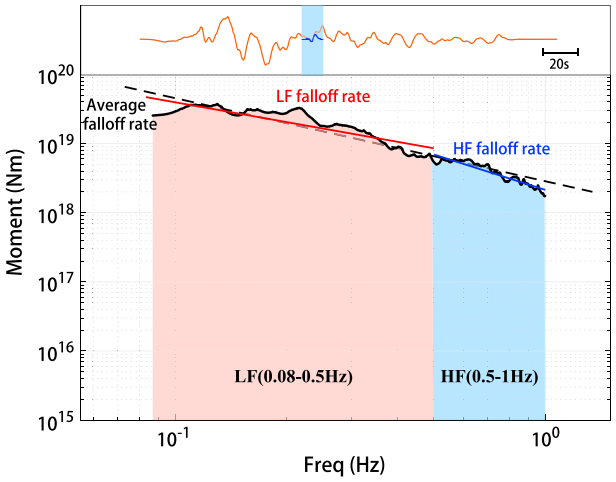

Figure 9. Cartoon to illustrate the method of time-varying spectral analysis. (top) A waveform in red and the tapered running short time window waveform in blue. (bottom) The recovered source spectra (black line) within the time window. Red and blue shaded areas indicate the two LF and HF frequency bands. Linear regressions are the best fit line for the spectrum from linear regression (red: LF; blue: HF; black dashed: overall).

radiated energy calculated from seismic data varies from 1.06×10^{16} J to 4.41×10^{17} J. While we find no clear break of slope in the source spectra that would justify using the double-corner frequency model (equation (14) and Figure 8), we use it to estimate the proportion of radiated energy in the missing frequency bands, below 0.08 Hz and that above 2 Hz. We find that our estimate is 71.2% of the total radiated energy, and thus, our value slightly underestimates the one we would find if we had a broader frequency bandwidth. Nevertheless, our value is larger than that found by Ye et al. (2015) ($2.2–3.15 \times 10^{16}$ J) and by the IRIS products (3.21×10^{16} J from IRIS DMC, 2013, last accessed 11 July 2017). Our choice of elastic structure (wave speed model) does not explain this difference. Therefore, we argue that the shape of the source spectrum, probably controlled by our use of empirical Green's function, can explain our overall higher estimate of radiated energy.

3.4. Time-Varying Spectral Analysis

3.4.1. Methodology

The previous parts of spectral analysis used the whole *P* wave train to provide the overall source information on the M_w 8.3 Illapel Earthquake. To obtain more detailed information during the rupture itself, we perform a time-varying analysis with robust estimations of radiated energy and parameterization of the spectrograms. Because we retrieve time-dependent dynamic source parameters (radiated energy and falloff rates), we can directly interpret these metrics with the ImCS-BP results.

We slide a 12 s long Hanning taper through the waveform of the mainshock with a 10 s overlap and a 2 s time step (Figure 9, top) and calculate the amplitude spectrum of the truncated window. Then, we remove the path effects by dividing the amplitude spectra with the eGfs spectra, since we assume that the Green's function remains the same during the earthquake. Therefore, for each time window, we can measure a band-limited source spectrum (Figure 9, bottom). We first average the time-dependent source spectra within each azimuth bin over the stations in order to investigate the azimuthal and temporal variations. In a last step, we stack the azimuth-averaged spectra to construct an overall spectrogram for this event. These source spectra can represent snap shots during the dynamic source process.

The minimum frequency of the spectrograms is 0.08 Hz, and we study the two frequency bands LF and HF to strictly compare with the results from ImCS-BP. We estimate the radiated energy evolution during the earthquake by applying equations (12) and (13) to each snapshot of the source spectrum and within the LF, HF, and the combined frequency band (0.08–1 Hz). Based on the radiated energy within each time window, we can estimate the average radiated energy rate (J/s) during that period (radiated energy divided by window length, that is, 12 s). Furthermore, we fit a simple linear regression to the spectrogram (log-spaced frequencies) and obtain the evolution of the falloff rate for the LF, HF, and the combined frequency bands (Figure 9, bottom). The two frequency bands LF and HF are narrow and are chosen arbitrarily to provide a low- and high-frequency bands well suited to the backprojection. A more rigorous analysis on the choice of frequency bands appropriate to the event size and to data constrained remains to be performed and is left for future work.

3.4.2. Results

Our temporal spectral analysis provides a unique view on the evolution in time of the source dynamic parameters. We show the source spectrogram, radiated energy rate, and falloff rate in Figure 10 within the same frequency bands (LF and HF) as the previous ImCS-BP results. Further details on the uncertainties can be found in Movie S1 in the supporting information. We limit our interpretation to the first 150 s, as the later phases, shown by the ImCS-BP results, are located in the outer-rise region and are probably not associated with the rupture process (Figures 10 and 11).

The radiated energy rate slowly increases in the stage I from the earthquake onset to 10 s, the stage that probably reflects the nucleation process. Most of the seismic energy is released during the stage II between 20 s and 100 s and presents two pronounced peaks at about 40 s and 60 s (Figure 10b). After 100 s, the total

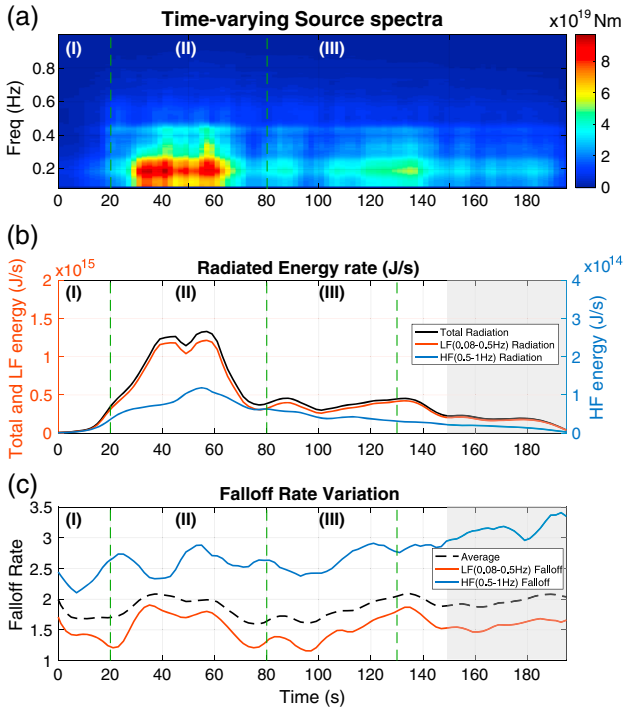

Figure 10. Results from the time-varying spectral analysis. (a) The time-varying source spectra in the time-frequency space. (b) Evolution of radiated energy with time: left *y* axis is for the total and LF radiated energy, while the right *y* axis is for the HF energy. (c) Evolution of falloff rates with time with similar color scheme as in Figure 10b. Black lines are averaged values, blue lines are the LF, and red lines are the HF results. Results after 150 s are shaded for not being representative of the evolution of the source. In all panels, green dashed lines and the roman numbers indicate the timings of the stages, 0–20 s, 20–100 s, and 100–200 s.

radiated energy rate stabilizes, and energy radiation finally dies until 200 s after the onset. We also integrate the obtained total radiated energy rate over time to have another estimation of total radiated energy within [0.08 1] Hz, which is 8.99×10^{16} J and comparable with that from total event spectrum 1.06×10^{17} J. Variations in radiated energy rate in the LF band are substantial. Because the LF radiation is very similar to the total radiation (as carried by the low-frequency moment level), the LF energy dominates and the two most energetic peaks seen in the total radiated energy are mostly carried by the low frequencies. This supports well our backprojection results (Figures 5a and 5b). Variations in radiated energy in the HF band are smoother than those of the LF band. The overall HF energy steeply increases from onset to 20 s, peaks at 50–60 s, and dies after that. This is very consistent with our HF backprojection results (Figures 5c and 5d).

The patterns of time-varying falloff rates from our observations are intriguing (Figure 10c). Because of our choice of regression scheme, LF and HF falloff rates are independent measures of spectral slope. It is important to remember that a low falloff rate is equivalent to a high ratio of high-frequency to low-frequency radiation. We show in Figure 10c the variations of falloff rate from the limited frequency bandwidths LF, HF, and from the combined bandwidth (called average falloff rate here). In the first stage, a general decrease appears at all frequency bands, indicating an increase in high-frequency content, which concurs with the nucleation inferred from radiated energy (Figure 10b).

At the beginning of stage II, LF and HF falloff rates appear to be anticorrelated. The LF falloff reaches a minimum at 22 s and peaks at 35 s during the overall steep growth in LF radiated energy. In contrast, HF falloff peaks at 24 s, which corresponds well with the rapid growth in HF energy. Both falloffs are similar at 40 s (peak of seismic radiation), favoring a smooth spectral shape with a single falloff. After 50 s and during stage III, both LF and HF falloff rates seem to vary together until the end of the rupture. Additionally, while there is no obvious correlation between HF falloff rate and radiated energy, LF falloff rate and radiated energy share similar variations. If there is no systematic correlation between radiated energy and falloff rates, understanding the contributions of low against high frequencies during the rupture and to the radiation of seismic wave is a metric that can be tested with dynamic source simulations.

We further detail the evolution of our three metrics of radiated energy (LF, HF, and combined) by exploring their variations with azimuth. Figure 11 shows the time varying radiated energy rates averaged over 10° azimuth bins that have at least 10 stations per bin. Unfortunately, there is a clear lack of data coverage at azimuths where we expect the source directivity. The features common to all azimuths are two energy peaks 1 and 2 in the LF and broadband time series, consistent with what we find previously (Figures 5a, 5b, and 10b). The difference in time interval between the peaks is indicators of source directivity, somewhat in a similar way to source time function analysis.

Focusing on the LF radiation, there are at least three coherent energy peaks (labeled 1, 2, and 3 in Figure 11b). The time interval between 0 and peak 1 is shorter at azimuth 30°, corresponding to the northeastward propagation of the rupture observed by the backprojection results (Figures 5a and 5b). The time interval between peak 1 and 3 around azimuths 320°–350° corresponds well to the northwestward rupture in the LF backprojection results. It is, however, not well constrained because of a data gap between 200° and 320° and the energy peak 3 is not clearly observed by stations within 320°–350°.

In contrast to the LF radiation, the HF radiation is simple. We estimate only a single coherent peak (labeled as 1) and the directivity toward azimuth 50° is obvious, which is also supported by backprojection results (Figures 5c and 5d).

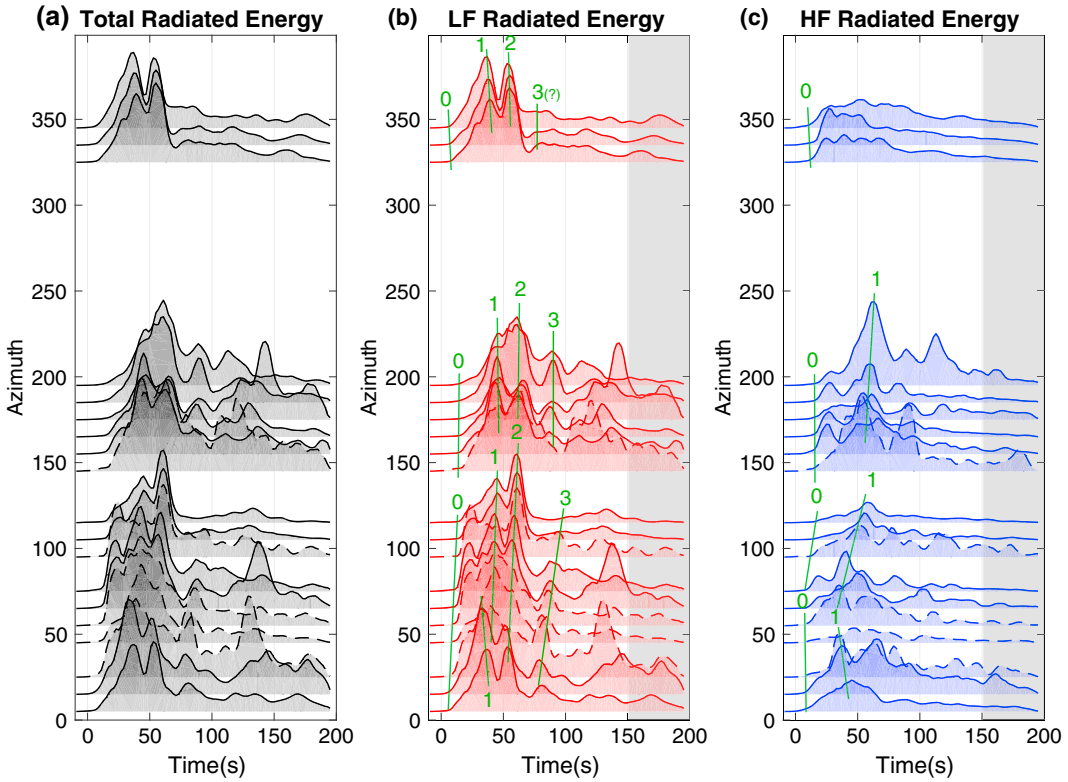

Figure 11. Time-varying radiated energy estimated at 10° azimuth bin: (a) total radiated energy, (b) LF radiated energy, and (c) HF radiated energy. Green thin lines and numbering indicate reference and indexing for the coherent radiated energy peaks. Results after 150 s are shaded for being less reliably interpretable to source processes.

4. Discussion

4.1. Integrated Source Analysis for the 2015 Illapel Earthquake

In stage I of this earthquake (0–20 s), ImCS-BP results show that both LF and HF energy bursts cluster around the epicenter the first 10 s (Figure 5). During this period, the time-varying spectral analysis results also present a weak increase of radiated energy (Figure 10b) and in the proportion of high frequencies through a decrease in the falloff rate from 2 to 1.7 (Figure 10c). During this stage, the rupture velocity curves provided by the LF energy bursts may also indicate a slow growth with, if interpreted as such, earthquake rupture velocities under 1 km/s (see Figure 6). This stage may be a signature of a slow initiation with a nucleation length scale of about 10 km. Ohnaka (2000) proposes a scaling that relates seismic moment with nucleation zone size that $M_0 = 1 \times 10^9 (2L_c)^3$, where M_0 and L_c are the seismic moment (Nm) and nucleation zone size (m), respectively. This scaling suggests a size of nucleation zone $L_c \approx 7.4$ km for the Illapel Earthquake. Although the question of whether the nucleation of earthquake is scale dependent or independent is still under debate (e.g., Ellsworth & Beroza, 1995; Lapusta & Rice, 2003; Meier et al., 2016; Olson & Allen, 2005), our observations seem to be consistent with Ohnaka (2000).

As mentioned in the previous section, we define stage II as the period of time between 20 s and 100 s. Our integrated analysis during this stage brings up many aspects of this rupture. Based on the LF ImCS-BP results, there are two distinct energy bursts North-West to the epicenter around 45–60 s and 60–80 s after onset (Figures 5a, 5b, and 6a). They correspond to the largest amplitudes of the velocity waveforms at about 40 s and 60 s (supporting information Figure S1) and to the two radiated energy peaks from our time-dependent spectral analysis results (Figures 10b and 11b).

Our integrated results show that most of the seismic radiated energy is released between 40 s and 80 s and their location is implied by the location of LF energy bursts (Figure 5b). Furthermore, the LF ImCS-BP results possibly indicate two changes in rupture velocity around 50 s and 80 s (Figure 6a). These velocity changes are well timed with the peaks of the backprojection energy bursts and radiated energy from spectral analysis.

This supports that changes in rupture velocity excite high-frequency radiation (Madariaga, 1977). Yin et al. (2016) compared the CS-BP results with various slip inversion models for this earthquake and highlighted that most of the LF energy bursts were located within the high slip regions, which are common to most slip models (e.g., Heidarzadeh et al., 2015; Ye et al., 2015). Melgar et al. (2016) also showed that their low-frequency backprojection results consistently overlapped with the large slip regions, indicating a relation between low-frequency backprojection results and coseismic slip.

There are about 10 s difference between the timing of the peaks of ImCS-BP energy burst (peaks at about 50 and 80 s, Figure 6a) and the peaks of the source spectrogram analysis (peaks at about 40 and 60 s, Figure 10b). As the rupture approaches the seismic array (USArray in this study), the seismic waves arrive earlier because of the shorter traveling distance. If the rupture propagation is left ignored, it will bring errors into the timing of the source (Figure 10). However, the ImCS-BP method can correct these source time shifts/errors and provide more accurate source time estimations. We refer to Yin and Yao (2016) for the details and test on this correction.

Directivity effects are inferred from both the evolution of radiated energy (with time and azimuth (Figure 11b) and from backprojected images: the time interval between the onset of radiation (0) and the first energy peak (1) shortens at azimuths 30°–50°, implying a probable direction of the rupture propagation similar to that found by the ImCS-BP (Figures 5a and 5b). Although the ImCS-BP results indicate a clear northwestern propagation toward the trench (azimuth of about 320°) from 30 s to 80 s (Figures 5a and 5b), there is no station available in the azimuth ranges of 200°–320° and 120°–140° to support directivity with the spectral analysis. This justifies well the use of backprojection techniques as a complement to spectral analysis to evaluate source directivity.

In contrast to the low-frequency radiation, the HF results from ImCS-BP show a propagation direction to the North-East (azimuth ~30°–50°), with a downdip unilateral propagation and a peak of coherence at 40–60 s. The HF peak time of radiated energy and source directivity inferred from backprojection are well consistent (Figures 10b and 11c).

Supported by both backprojection and spectral analyses, the main characteristic of the seismic radiation of this earthquake is the obvious discrepancy in the evolution of the low- and high-frequency content during the rupture. They may represent two processes of dynamic rupture characterized by different time scales (inverse of frequency) at the updip and at the downdip part of the megathrust. The different rupture behaviors at the updip and downdip regions have also been observed by Melgar et al. (2016). They interpret the shallow part to behave similarly to a tsunami earthquake (Kanamori, 1972), whereas the deeper portion would behave like a "normal" source. We will discuss possible dynamic mechanisms for this phenomenon in section 4.2.1.

Finally, we ought to discuss during the stage III, beyond 100 s into the rupture. Lee et al. (2016) suggest that this event is a very long lasting earthquake (duration ~250 s), as a combination of a megathrust earthquake that propagates updip in the first 150 s and a tsunami earthquake (size ~M_w 8.08) that propagates along the trench with a slow rupture speed from 150 s to 250 s. However, the ImCS-BP low-frequency energy bursts are clearly located on the outer-rise region (Figures 5a and 5b) rather than along the trench. As discussed by Yue et al. (2017), these outer-rise energy bursts are probably introduced by the coherent coda signals due to late water reverberations. The source spectrograms clearly show peaks around 0.1 Hz, which corresponds to 10 s (Figure 8), which supports the results from Yue et al. (2017). Therefore, these outer-rise bursts revealed by ImCS-BP likely arise from reverberations in the water column. Therefore, stage III does not seem to be related to the rupture but rather a wave propagation effect in the outer-rise region.

4.2. Physical Interpretations

4.2.1. Observations of Depth-Dependent Radiation for Point Sources

The spatiotemporal distribution of seismic energy bursts from ImCS-BP potentially brings insight on physical properties on the fault interface. Many backprojection studies of the large subduction zone thrust earthquakes, such as the M_w 9.3 2004 and M_w 8.8 2005 Sumatra, the M_w 9.0 2011 Japan, the M_w 8.8 2010 and M_w 8.3 2015 southern Chile (Lay et al., 2012; Wang & Mori, 2011; Yao et al., 2011, 2013; Yin et al., 2016), the M_w 8.0 2007 Peru (Sufri et al., 2012), and in a large continental subduction zone such as the M_w 7.9 2015 Nepal (Yin et al., 2017; Yue et al., 2016), reveal clear systematic differences between the frequency content

of the updip and downdip regions. Our results from ImCS-BP are consistent with previous studies that identify LF radiation in the updip part and HF radiation in the downdip region of the megathrust earthquakes.

Other observations confirm the depth-varying seismic radiation in subduction zone earthquakes. It is observed from small and moderate shallow (<50 km) earthquakes on the megathrust. Houston (2001) found a trend in source time functions that, when adjusted to the seismic moment scaling with source duration, shorten as source depth increases, implying a higher frequency content. Denolle and Shearer (2016) find a similar trend in Japan and in Sumatra for moderate and large events, trend also confirmed by Ko and Kuo (2016) for a wide range of earthquake magnitudes in the Japan trench. Bilek and Lay (1999) interpret this shortening of source pulses as a systematic variation in rigidity with depth. Furthermore, studies on the generation of high-frequency strong ground motion simplify the source of megathrust earthquakes to localized strong motion generation areas that often locate downdip of the fault (e.g., Asano & Iwata, 2012; Ruiz et al., 2012).

Regarding any systematic changes in high-frequency falloff rate with depth, Ye et al. (2016) argue for a decrease in high-frequency falloff rates with depth for M_w 7+ in subduction zones, implying a high ratio of high- to low-frequency radiation for the deeper parts of the megathrust. However, Ko and Kuo (2016) find in the Japan trench a relatively constant radiation efficiency with depth, and given the observations of increase stress drop with depth, the high-frequency falloff rates should at most remain constant with depth. The contradictions in these results highlight a need to better estimate the high-frequency falloff rates.

4.2.2. Time-Varying Spectral Falloff Rates

The spectral falloff rate controls the attenuation of high frequency of the source time functions. Aki (1967) proposes a statistical model with two correlation lengths that predict a spectral model with a high-frequency asymptote of ω^{-2}. Dynamical models of cracks indicate that stopping phases, which effectively corresponds to an abrupt change in rupture velocity, give an upper bound in high-frequency radiation with falloffs of $n = 2$ and smoother changes should excite high-frequency radiation with falloffs of $n > 2$ (Madariaga, 1977). The more recent study of Kaneko and Shearer (2014) finds that the high-frequency falloff rate varies between 1.5 and 2.5 for far-field *P* waves with all azimuth and takeoff angles relevant to teleseismic measurements (0°–40° in takeoff angles). Therefore, great variations in n can come from simple and known dynamics of earthquake rupture.

Moreover, various canonical and kinematic slip rate functions (review in Tinti et al., 2005) exhibit various spectral falloff rates (supporting information Figure S9), for example, the Yoffe function has a falloff of 1, the triangle function has a falloff rate of 2. Dynamically consistent slip rate functions can relate to dynamic parameters (Piatanesi et al., 2004; Tinti et al., 2005), and Tinti et al. (2005) propose a dynamically consistent slip rate function with a falloff rate greater than 2. Kinematic parametrization (see Schmedes et al., 2010, and Crempien & Archuleta, 2014, for details of methodology of the parameterization) with a fixed slip rate function shape yields a source spectrogram with a falloff rate that is constant in time (supporting information Figure S10). Our observations and those of Denolle et al. (2015) suggest otherwise. Therefore, future investigation through dynamic rupture simulation is necessary to explain the temporal evolution of high-frequency falloff rates.

4.2.3. Prediction of Depth-Dependence Radiation From Earthquake Dynamics

The first mechanism that can explain depth dependence in seismic radiation is the stress conditions on the fault before the rupture. Prestress and its heterogeneity are particularly difficult to establish, as multicycle earthquakes simulations require both long-term fault healing and short-term dynamics (Duan & Oglesby, 2005, 2007). The frequency dependence of the seismic radiation during the Tohoku earthquake has been explained by both 2-D and 3-D dynamic simulations though heterogeneous distribution prestress on the fault surface (Huang et al., 2012, 2014; Galvez et al., 2014).

A second mechanism that can explain the depth dependence in the frequency of seismic radiation is the frictional resistance on the fault interface. The phase transformation of the minerals constituting the near fault fabric alters their frictional properties (Lay et al., 2012; Scholz, 1998; Yao et al., 2013). Parametrization of friction, either through velocity- (Dieterich, 1992, 1994; Rice et al., 2001; Ruina, 1983) or slip-weakening (Andrews, 1976; Ida, 1972) laws, is often invoked through a characteristic or critical length scale that can be tuned (Huang et al., 2012, 2014; He et al., 2016; Yang & Weng, 2016) to simulate high-frequency radiation. Often the shallowest part of the plate interface is considered unfavorable to earthquake nucleation (Marone &

Saffer, 2007; Saffer & Marone, 2003), but other dynamic weakening mechanisms (flash heating and thermal pressurization; Noda & Lapusta, 2013; Rice, 2006; Viesca & Garagash, 2015) may allow propagation through those areas.

A third, but not least, mechanism is the geometry of the fault. The hanging wall, or accretionary wedge in subduction zone, undergoes large dynamic stresses during the rupture (Brune, 1996; Kozdon & Dunham, 2013; Ma, 2012; Nielsen, 1998; Oglesby et al., 1998). The materials in the accretionary wedge may thus respond inelastically to strong dynamic stresses, an effect that Ma and Hirakawa (2013) proposed to exaggerate the depth dependence to seismic radiation by reducing the high-frequency radiation at the trench. The accretionary prism, if described as inelastic, may act as an "energy sink," reducing the directivity effects in seismic radiation and absorbing the high-frequency radiation at the trench. Wedge failure may thus explain our observations.

Our observations alone cannot discriminate between these competing mechanisms. However, they provide reliable and novel constraints to validate dynamic rupture simulations and motivate the need to investigate the impact of each mechanism on seismic radiation.

4.2.4. Cracks or Self-Healing Pulses?

In our results from both backprojection and spectral analyses, the LF and HF seismic radiation differ in the location of their excitation and in the direction of their propagation. Both behave as if they occurred due to two different rupture processes. Our observations suggest a unilateral migration of the seismic radiation, either updip (LF radiation) or downdip (HF radiation). If interpreted independently, both results would favor interpretations of unilateral pulse-like ruptures, such as that of the M_w 7.9 2015 Nepal Earthquake (Avouac et al., 2015; Fan & Shearer, 2015; Galetzka et al., 2015; Grandin et al., 2015; Yin et al., 2017), but in opposite directions. However, we only observe a single dominant time scale in the whole event spectrum (the source duration), which favors a crack-like model, as against a pulse-like model that exhibits two time scales, the source duration and the risetime (Denolle & Shearer, 2016; Haskell, 1964). Because of this contrasting behavior of the radiation, it is difficult to assess whether the rupture had a more pulse-like behavior (such as a typical Haskell model) or a crack-like behavior. One possible explanation is an asymmetry in the slip rate function at the rupture front where, for the propagation of a simple crack front, the updip slip rate function is smoother (deficient in high frequencies) than the downdip slip rate function. Simulations of dynamic sources are also required to address this issue.

4.2.5. Tsunamigenesis

Our final discussion point is the spectral shape of the main event at low frequencies. Our strict SNR criterion at low frequency provides us confidence in the peculiar trough in the spectrum at 0.035 Hz, which made us ignore the 0.02–0.08 Hz frequency band in our spectral model fitting. This type of feature is similar to that observed during tsunami earthquakes (Abercrombie et al., 2001 (Java 1994 event); Ammon et al., 2006 (Java 2006 event); Lay et al., 2011 (Mentawai 2010 event); and Denolle & Shearer, 2016 (Mentawai 2010 and Java 2006 events)). While the tsunami generated by the Illapel event reached runups as high as 11 m (Melgar et al., 2016), it is possible that the spectral shape reflects some features common to tsunami earthquakes. To the best of our knowledge, there exists currently no physical explanation to this particular trough in *P* wave spectra of tsunami earthquake.

5. Conclusions

Our study presents new methodologies in backprojection and spectral analyses of large earthquakes that hopefully provide observational metrics relevant to megathrust earthquake dynamics. They are effective to analyze remote and offshore shallow earthquakes by accounting for phase and amplitude information of the complete *P* wave train (direct *P*, depth phases, and water reverberations). Both methods provide observational constraints on the evolution of the seismic radiation during the rupture and complement each other by combining reliable phase and amplitude information. Our multidimensional source analysis can provide the spatiotemporal evolution of seismic radiation during the earthquake, with the temporal evolution of radiated energy and varying falloff rates.

We applied both methods on the M_w 8.3 2015 Illapel Earthquake and found a distinct evolution of the low-frequency radiation compared to the high-frequency radiation. Not surprisingly, the low-frequency radiation is prominent in large earthquakes and appears consistently shallower than high-frequency radiation.

We hope that our combined approach to image the seismic radiation during the earthquake provides relevant metrics to bridge kinematic observations and dynamic models. Understanding the physical mechanisms that can explain our observations is central to improving our knowledge of large megathrust earthquakes. Different mechanisms (friction, prestress, and geometry) can produce variation with depth of the frequency content of seismic radiation. Determining whether one mechanism dominates over the others deserves to be addressed in the future research.

Acknowledgments
The authors sincerely appreciate the constructive comments from the JGR Associate Editor Jean-Paul Ampuero, Cheng Ji, and anonymous reviewer to help improve this manuscript. The authors also thank Linda M. Warren and Peter M. Shearer for providing the *t** model. The USArray seismic data for the ImCS-BP results are downloaded from IRIS-DMC (Incorporated Research Institutions for Seismology Data Management Center. Networks DOIs are the following: AZ: doi:10.7914/SN/AZ; BK: doi:10.9732/BDSN; CI: doi:10.7914/SN/CI; CN; II: doi:10.7914/SN/II; IM; IU: doi:10.7914/SN/IU; IW: doi:10.7914/SN/IW; LD; MX; N4: doi:10.7914/SN/N4; NM; OK: doi:10.7914/SN/OK; PB; PE: doi:10.7914/SN/PE; PY: doi:10.7914/SN/PY; SC; TA: doi:10.7914/SN/TA; US: doi:10.7914/SN/US; UU: doi:10.7914/SN/UU; YN: doi:10.7914/SN/YN_2010) using Wibler 3. The global data for the spectral analysis are from the Federal Digital Seismographs Network (FDSN. Networks DOIs are as follows: AF: doi:10.7914/SN/AF; AI: doi:10.7914/SN/AI; AU; AZ: doi:10.7914/SN/AZ; BK: doi:10.9732/BDSN; C1; CC: doi:10.7914/SN/CC; CI: doi:10.7914/SN/CI; CM; CN; CU: doi:10.7914/SN/CU; G: doi:10.18715/GEOSCOPE.G; GE: doi:10.14470/TR560404; GT: doi:10.7914/SN/GT; II: doi:10.7914/SN/II; IM; IU: doi:10.7914/SN/IU; IW: doi:10.7914/SN/IW; MB: doi:10.7914/SN/MB; MX; TA: doi:10.7914/SN/TA; TR) using Obspy (available at https://github.com/obspy/obspy/wiki). Most of the data processing, calculations, and figure plottings are carried out using Matlab. Some figures in the manuscript are also plotted using GMT (the Generic Mapping Tools, http://gmt.soest.hawaii.edu/projects/gmt/wiki/Download). This work is partially supported by National Natural Science Foundation of China (grant: 41374055).

References

Abercrombie, R. E., Antolik, M., Felzer, K., & Ekström, G. (2001). The 1994 Java tsunami earthquake: Slip over a subducting seamount. *Journal of Geophysical Research*, *106*(B4), 6595–6607. https://doi.org/10.1029/2000JB900403

Aki, K. (1967). Scaling law of seismic spectrum. *Journal of Geophysical Research*, *72*(4), 1217–1231. https://doi.org/10.1029/JZ072i004p01217

Akuhara, T., & Mochizuki, K. (2015). Hydrous state of the subducting Philippine Sea plate inferred from receiver function image using onshore and offshore data. *Journal of Geophysical Research: Solid Earth*, *120*, 8461–8477. https://doi.org/10.1002/2015JB012336

Allmann, B. P., & Shearer, P. M. (2009). Global variations of stress drop for moderate to large earthquakes. *Journal of Geophysical Research*, *114*, B01310. https://doi.org/10.1029/2008JB005821

Ammon, C. J., Kanamori, H., Lay, T., & Velasco, A. A. (2006). The 17 July 2006 Java tsunami earthquake. *Geophysical Research Letters*, *33*, L24308. https://doi.org/10.1029/2006GL028005

Andrews, D. J. (1976). Rupture propagation with finite stress in antiplane strain. *Journal of Geophysical Research*, *81*(20), 3575–3582. https://doi.org/10.1029/JB081i020p03575

Anon (2005). A densely distributed high-sensitivity seismograph network in Japan: Hi-net by National Research Institute for Earth Science and Disaster Prevention. *The Review of Scientific Instruments*, *76*, 21301. https://doi.org/10.1063/1.1854197

Asano, K., & Iwata, T. (2012). Source model for strong ground motion generation in the frequency range 0.1–10 Hz during the 2011 Tohoku earthquake. *Earth, Planets and Space*, *64*, 1111–1123. https://doi.org/10.5047/eps.2012.05.003

Avouac, J.-P., Meng, L., Wei, S., Wang, T., & Ampuero, J.-P. (2015). Lower edge of locked Main Himalayan Thrust unzipped by the 2015 Gorkha earthquake. *Nature Geoscience*, *8*(9), 708–711. https://doi.org/10.1038/ngeo2518

Baltay, A. S., Beroza, G. C., & Ide, S. (2014). Radiated energy of great earthquakes from teleseismic empirical Green's function deconvolution. *Pure and Applied Geophysics*, *171*(10), 2841–2862. https://doi.org/10.1007/s00024-014-0804-0

Bernard, P., & Madariaga, R. (1984). High-frequency seismic radiation from a buried circular fault. *Geophysical Journal of the Royal Astronomical Society*, *78*(1), 1–17. https://doi.org/10.1111/j.1365-246X.1984.tb06468.x

Beyreuther, M., Barsch, R., Krischer, L., Megies, T., Behr, Y., & Wassermann, J. (2010). ObsPy: A Python toolbox for seismology. *Seismological Research Letters*, *81*, 530–533. https://doi.org/10.1785/gssrl.81.3.530

Bilek, S. L., & Lay, T. (1999). Rigidity variations with depth along interplate megathrust faults in subduction zones. *Nature*, *400*(6743), 443–446. https://doi.org/10.1038/22739

Boatwright, J. (1980). A spectral theory for circular seismic sources; simple estimates of source dimension, dynamic stress drop, and radiated seismic energy. *Bulletin of the Seismological Society of America*, *70*(1), 1–27.

Boyd, S., & Vandenberghe, L. (2004). *Convex Optimization*. Cambridge, UK: Cambridge University Press. https://doi.org/10.1017/CBO9780511804441

Brown, L., Wang, K., & Sun, T. (2015). Static stress drop in the M_w 9 Tohoku-oki earthquake: Heterogeneous distribution and low average value. *Geophysical Research Letters*, *42*(24), 10,595–10,600. https://doi.org/10.1002/2015GL066361

Brune, J. N. (1996). Particle motions in a physical model of shallow angle thrust faulting. *Proceedings of the Indian Academy of Sciences, Earth and Planetary Sciences*, *105*(2), 197–206. https://doi.org/10.1007/BF02876014

Brune, J. N. (1970). Tectonic stress and the spectra of seismic shear waves from earthquakes. *Journal of Geophysical Research*, *75*(26), 4997–5009. https://doi.org/10.1029/JB075i026p04997

Brune, J. N. (1971). Correction (to Brune, 1970). *Journal of Geophysical Research*, *76*, 5002.

Candès, E. J., Romberg, J. K., & Tao, T. (2006). Stable signal recovery from incomplete and inaccurate measurements. *Communications on Pure and Applied Mathematics*, *59*, 1207–1223. https://doi.org/10.1002/cpa.20124

Crempien, J. G. F., & Archuleta, R. J. (2014). UCSB method for simulation of broadband ground motion from kinematic earthquake sources. *Seismological Research Letters*, *86*(1), 61–67. https://doi.org/10.1785/0220140103

Denolle, M. A., Fan, W., & Shearer, P. M. (2015). Dynamics of the 2015 *M*7.8 Nepal earthquake. *Geophysical Research Letters*, *42*, (18), 7467–7475. https://doi.org/10.1002/2015GL065336

Denolle, M. A., & Shearer, P. M. (2016). New perspectives on self-similarity for shallow thrust earthquakes. *Journal of Geophysical Research: Solid Earth*, *121*, 6533–6565. https://doi.org/10.1002/2016JB013105

Dieterich, J. H. (1992). Earthquake nucleation on faults with rate-and state-dependent strength. *Tectonophysics*, *211*(1-4), 115–134. https://doi.org/10.1016/0040-1951(92)90055-B

Dieterich, J. (1994). A constitutive law for rate of earthquake production and its application to earthquake clustering. *Journal of Geophysical Research*, *99*(B2), 2601–2618. https://doi.org/10.1029/93JB02581

Donoho, D. L. (2006). Compressed sensing. *IEEE Transactions on Information Theory*, *52*, 1289–1306. https://doi.org/10.1109/TIT.2006.871582

Duan, B., & Oglesby, D. D. (2005). Multicycle dynamics of nonplanar strike-slip faults. *Journal of Geophysical Research*, *110*, B03304. https://doi.org/10.1029/2004JB003298

Duan, B., & Oglesby, D. D. (2007). Nonuniform prestress from prior earthquakes and the effect on dynamics of branched fault systems. *Journal of Geophysical Research*, *112*, B05308. https://doi.org/10.1029/2006JB004443

Dziewonski, A. M., & Anderson, D. L. (1981). Preliminary reference Earth model. *Physics of the Earth and Planetary Interiors*, *25*(4), 297–356. https://doi.org/10.1016/0031-9201(81)90046-7

Ekström, G., Nettles, M., & Dziewoński, A. M. (2012). The global CMT project 2004–2010: Centroid-moment tensors for 13,017 earthquakes. *Physics of the Earth and Planetary Interiors*, *200-201*, 1–9. https://doi.org/10.1016/j.pepi.2012.04.002

Ellsworth, W. L., & Beroza, G. C. (1995). Seismic evidence for an earthquake nucleation phase. *Science*, *268*(5212), 851–855. https://doi.org/10.1126/science.268.5212.851

Eshelby, J. D. (1957). The determination of the elastic field of an ellipsoidal inclusion, and related problems. In *Proceedings of the Royal Society of London A: Mathematical, Physical and Engineering Sciences* (Vol. 241, pp. 376–396).

Fan, W., & Shearer, P. M. (2015). Detailed rupture imaging of the 25 April 2015 Nepal earthquake using teleseismic *P* waves. *Geophysical Research Letters*, *42*(14), 5744–5752. https://doi.org/10.1002/2015GL064587

Fan, W., & Shearer, P. M. (2016). Local near instantaneously dynamically triggered aftershocks of large earthquakes. *Science*, *353*(6304), 1133–1136. https://doi.org/10.1126/science.aag0013

Fukahata, Y., Yagi, Y., & Rivera, L. (2014). Theoretical relationship between back-projection imaging and classical linear inverse solutions. *Geophysical Journal International*, *196*(1), 552–559. https://doi.org/10.1093/gji/ggt392

Galetzka, J., Melgar, D., Genrich, J. F., Geng, J., Owen, S., Lindsey, E. O., … Maharjan, N. (2015). Slip pulse and resonance of the Kathmandu basin during the 2015 Gorkha earthquake, Nepal. *Science*, *349*(6252), 1091–1095. https://doi.org/10.1126/science.aac6383

Galvez, P., Ampuero, J.-P., Dalguer, L. A., Somala, S. N., & Nissen-Meyer, T. (2014). Dynamic earthquake rupture modelled with an unstructured 3-D spectral element method applied to the 2011 *M*9 Tohoku earthquake. *Geophysical Journal International*, *198*(2), 1222–1240. https://doi.org/10.1093/gji/ggu203

Grandin, R., Vallée, M., Satriano, C., Lacassin, R., Klinger, Y., Simoes, M., & Bollinger, L. (2015). Rupture process of the M_w = 7.9 2015 Gorkha earthquake (Nepal): Insights into Himalayan megathrust segmentation. *Geophysical Research Letters*, *42*(20), 8373–8382. https://doi.org/10.1002/2015GL066044

Hanks, T. C. (1979). b values and $\omega-\gamma$ seismic source models: Implications for tectonic stress variations along active crustal fault zones and the estimation of high-frequency strong ground motion. *Journal of Geophysical Research*, *84*(B5), 2235–2242. https://doi.org/10.1029/JB084iB05p02235

Haskell, N. A. (1964). Total energy and energy spectral density of elastic wave radiation from propagating faults. *Bulletin of the Seismological Society of America*, *54*(6A), 1811–1841.

Hayes, G. P., Wald, D. J., & Johnson, R. L. (2012). Slab1.0: A three-dimensional model of global subduction zone geometries. *Journal of Geophysical Research*, *117*, B01302. https://doi.org/10.1029/2011JB008524

He, B., Yang, H., & Weng, H. (2016). Rupture process of the 2012 Nicoya earthquake inferred from interseismic locking distributions. In: 2016 AOGS Annual Meeting Abstracts.

Heidarzadeh, M., Murotani, S., Satake, K., Ishibe, T., & Gusman, A. R. (2015). Source model of the 16 September 2015 Illapel, Chile M_w 8.4 earthquake based on teleseismic and tsunami data. *Geophysical Research Letters*, *43*(2), 643–650. https://doi.org/10.1002/2015GL067297

Houston, H. (2001). Influence of depth, focal mechanism, and tectonic setting on the shape and duration of earthquake source time functions. *Journal of Geophysical Research*, *106*(B6), 11,137–11,2150. https://doi.org/10.1029/2000JB900468

Houston, H., & Kanamori, H. (1986). Source spectra of great earthquakes: Teleseismic constraints on rupture process and strong motion. *Bulletin of the Seismological Society of America*, *76*(1), 19–42.

Huang, Y., Ampuero, J.-P., & Kanamori, H. (2014). Slip-weakening models of the 2011 Tohoku-Oki earthquake and constraints on stress drop and fracture energy. *Pure and Applied Geophysics*, *171*(10), 2555–2568. https://doi.org/10.1007/s00024-013-0718-2

Huang, Y., Meng, L., & Ampuero, J.-P. (2012). A dynamic model of the frequency-dependent rupture process of the 2011 Tohoku-Oki earthquake. *Earth, Planets and Space*, *64*(12), 1061–1066. https://doi.org/10.5047/eps.2012.05.011

Husseini, M. I. (1977). Energy balance for motion along a fault. *Geophysical Journal International*, *49*(3), 699–714. https://doi.org/10.1111/j.1365-246X.1977.tb01313.x

Ida, Y. (1972). Cohesive force across the tip of a longitudinal-shear crack and Griffith's specific surface energy. *Journal of Geophysical Research*, *77*(20), 3796–3805. https://doi.org/10.1029/JB077i020p03796

Incorporated Research Institutions for Seismology Data Management Center (IRIS DMC) (2011). Data Services Products: Back-projection *P*-wave back-projection rupture imaging. https://doi.org/10.17611/DP/BP.1

Incorporated Research Institutions for Seismology Data Management Center (IRIS DMC) (2013). Data Services Products: EQEnergy Earthquake energy & rupture duration. https://doi.org/10.17611/DP/10095476

Ishii, M., Shearer, P. M., Houston, H., & Vidale, J. E. (2005). Extent, duration and speed of the 2004 Sumatra–Andaman earthquake imaged by the Hi-Net array. *Nature*, *435*(7044), 933–936. https://doi.org/10.1038/nature03675

Ishii, M., Shearer, P. M., Houston, H., & Vidale, J. E. (2007). Teleseismic *P* wave imaging of the 26 December 2004 Sumatra-Andaman and 28 March 2005 Sumatra earthquake ruptures using the Hi-net array. *Journal of Geophysical Research*, *112*, B11307. https://doi.org/10.1029/2006JB004700

Ji, C., Wald, D. J., & Helmberger, D. V. (2002a). Source description of the 1999 Hector Mine, California, earthquake, Part I: Wavelet domain inversion theory and resolution analysis. *Bulletin of the Seismological Society of America*, *92*(4), 1192–1207. https://doi.org/10.1785/0120000916

Ji, C., Wald, D. J., & Helmberger, D. V. (2002b). Source description of the 1999 Hector Mine, California, earthquake, Part II: Complexity of slip history. *Bulletin of the Seismological Society of America*, *92*(4), 1208–1226. https://doi.org/10.1785/0120000917

Kanamori, H. (1972). Mechanism of tsunami earthquakes. *Physics of the Earth and Planetary Interiors*, *6*(5), 346–359. https://doi.org/10.1016/0031-9201(72)90058-1

Kaneko, Y., & Shearer, P. M. (2014). Seismic source spectra and estimated stress drop derived from cohesive-zone models of circular subshear rupture. *Geophysical Journal International*, *197*(2), 1002–1015. https://doi.org/10.1093/gji/ggu030

Kennett, B. L. N., & Engdahl, E. R. (1991). Traveltimes for global earthquake location and phase identification. *Geophysical Journal International*, *105*(2), 429–465. https://doi.org/10.1111/j.1365-246X.1991.tb06724.x

Kikuchi, M., & Kanamori, H. (1982). Inversion of complex body waves. *Bulletin of the Seismological Society of America*, *72*(2), 491–506.

Kikuchi, M., & Kanamori, H. (1986). Inversion of complex body waves-II. *Physics of the Earth and Planetary Interiors*, *43*(3), 205–222. https://doi.org/10.1016/0031-9201(86)90048-8

Kikuchi, M., & Kanamori, H. (1991). Inversion of complex body waves—III. *Bulletin of the Seismological Society of America*, *81*(6), 2335–2350.

Kiser, E., Ishii, M., Langmuir, C. H., Shearer, P. M., & Hirose, H. (2011). Insights into the mechanism of intermediate-depth earthquakes from source properties as imaged by back projection of multiple seismic phases. *Journal of Geophysical Research*, *116*, B06310. https://doi.org/10.1029/2010JB007831

Ko, J. Y.-T., & Kuo, B.-Y. (2016). Low radiation efficiency of the intermediate-depth earthquakes in the Japan subduction zone. *Geophysical Research Letters*, *43*, 11,611–11,619. https://doi.org/10.1002/2016GL070993

Kozdon, J. E., & Dunham, E. M. (2013). Rupture to the trench: Dynamic rupture simulations of the 11 March 2011 Tohoku earthquake. *Bulletin of the Seismological Society of America*, *103*(2B), 1275–1289. https://doi.org/10.1785/0120120136

Lapusta, N., & Rice, J. R. (2003). Nucleation and early seismic propagation of small and large events in a crustal earthquake model. *Journal of Geophysical Research*, *108*(B4), 2205. https://doi.org/10.1029/2001JB000793

Lay, T., Ammon, C. J., Kanamori, H., Yamazaki, Y., Cheung, K. F., & Hutko, A. R. (2011). The 25 October 2010 Mentawai tsunami earthquake (M_w 7.8) and the tsunami hazard presented by shallow megathrust ruptures. *Geophysical Research Letters*, *38*, L06302. https://doi.org/10.1029/2010GL046552

Lay, T., Kanamori, H., Ammon, C. J., Koper, K. D., Hutko, A. R., Ye, L., … Rushing, T. M. (2012). Depth-varying rupture properties of subduction zone megathrust faults. *Journal of Geophysical Research*, *117*, B04311. https://doi.org/10.1029/2011JB009133

Lee, S.-J., Yeh, T.-Y., Lin, T.-C., Lin, Y.-Y., Song, T.-R. A., & Huang, B.-S. (2016). Two-stage composite megathrust rupture of the 2015 M_w 8.4 Illapel, Chile, earthquake identified by spectral-element inversion of teleseismic waves. *Geophysical Research Letters*, *43*(10), 4979–4985. https://doi.org/10.1002/2016GL068843

Li, L., Lay, T., Cheung, K. F., & Ye, L. (2016). Joint modeling of teleseismic and tsunami wave observations to constrain the 16 September 2015 Illapel, Chile, M_w 8.3 earthquake rupture process. *Geophysical Research Letters*, *43*, 4303–4312. https://doi.org/10.1002/2016GL068674

Ma, S. (2012). A self-consistent mechanism for slow dynamic deformation and tsunami generation for earthquakes in the shallow subduction zone. *Geophysical Research Letters*, *39*, L11310. https://doi.org/10.1029/2012GL051854

Ma, S., & Hirakawa, E. T. (2013). Dynamic wedge failure reveals anomalous energy radiation of shallow subduction earthquakes. *Earth and Planetary Science Letters*, *375*, 113–122. https://doi.org/10.1016/j.epsl.2013.05.016

Madariaga, R. (1976). Dynamics of an expanding circular fault. *Bulletin of the Seismological Society of America*, *66*(3), 639–666.

Madariaga, R. (1977). High-frequency radiation from crack (stress drop) models of earthquake faulting. *Geophysical Journal International*, *51*(3), 625–651. https://doi.org/10.1111/j.1365-246X.1977.tb04211.x

Madariaga, R., Ampuero, J. P., & Adda-Bedia, M. (2006). Seismic radiation from simple models of earthquakes. In R. Abercrombie, et al. (Eds.), *Earthquakes: Radiated Energy and the Physics of Faulting* (pp. 223–236). Washington, DC: American Geophysical Union. https://doi.org/10.1029/170GM23

Mai, P. M., Schorlemmer, D., Page, M., Ampuero, J. P., Asano, K., Causse, M., … Zielke, O. (2016). The earthquake-source inversion validation (SIV) project. *Seismological Research Letters*, *87*(3), 690–708. https://doi.org/10.1785/0220150231

Marone, C., & Saffer, D. M. (2007). Fault friction and the upper transition from seismic to aseismic faulting. In T. H. Dixon & J. C. Moore (Eds.), *Seismogenic Zone Subduction Thrust Faults* (pp. 346–369). New York: Columbia University Press. https://doi.org/10.7312/dixo13866-012

Meier, M.-A., Heaton, T., & Clinton, J. (2016). Evidence for universal earthquake rupture initiation behavior. *Geophysical Research Letters*, *43*, 7991–7996. https://doi.org/10.1002/2016GL070081

Melgar, D., Fan, W., Riquelme, S., Geng, J., Liang, C., Fuentes, M., … Fielding, E. J. (2016). Slip segmentation and slow rupture to the trench during the 2015, M_w 8.3 Illapel, Chile earthquake. *Geophysical Research Letters*, *43*, 961–966. https://doi.org/10.1002/2015GL067369

Meng, L., Ampuero, J.-P., Luo, Y., Wu, W., & Ni, S. (2012). Mitigating artifacts in back-projection source imaging with implications for frequency-dependent properties of the Tohoku-Oki earthquake. *Earth, Planets and Space*, *64*, 1101–1109. https://doi.org/10.5047/eps.2012.05.010

Meng, L., Inbal, A., & Ampuero, J.-P. (2011). A window into the complexity of the dynamic rupture of the 2011 M_w 9 Tohoku-Oki earthquake. *Geophysical Research Letters*, *38*, L00G07. https://doi.org/10.1029/2011GL048118

Miyake, H., Iwata, T., & Irikura, K. (2003). Source characterization for broadband ground-motion simulation: Kinematic heterogeneous source model and strong motion generation area. *Bulletin of the Seismological Society of America*, *93*(6), 2531–2545. https://doi.org/10.1785/0120020183

Nielsen, S. B. (1998). Free surface effects on the propagation of dynamic rupture. *Geophysical Research Letters*, *25*(1), 125–128. https://doi.org/10.1029/97GL03445

Noda, H., & Lapusta, N. (2013). Stable creeping fault segments can become destructive as a result of dynamic weakening. *Nature*, *493*(7433), 518–521. https://doi.org/10.1038/nature11703

Oglesby, D. D., Archuleta, R. J., & Nielsen, S. B. (1998). Earthquakes on dipping faults: The effects of broken symmetry. *Science*, *280*(5366), 1055–1059. https://doi.org/10.1126/science.280.5366.1055

Ohnaka, M. (2000). A physical scaling relation between the size of an earthquake and its nucleation zone size. In *Microscopic and Macroscopic Simulation: Towards Predictive Modelling of the Earthquake Process* (pp. 2259–2282). Basel: Birkhäuser. https://doi.org/10.1007/978-3-0348-7695-7_24

Okada, Y., Kasahara, K., Hori, S., Obara, K., Sekiguchi, S., Fujiwara, H., & Yamamoto, A. (2004). Recent progress of seismic observation networks in Japan —Hi-net, F-net, K-NET and KiK-net—. *Earth, Planets and Space*, *56*, xv–xxviii. https://doi.org/10.1186/BF03353076

Olson, E. L., & Allen, R. M. (2005). The deterministic nature of earthquake rupture. *Nature (London)*, *438*, 212–215. https://doi.org/10.1038/nature04214

Piatanesi, A., Tinti, E., Cocco, M., & Fukuyama, E. (2004). The dependence of traction evolution on the earthquake source time function adopted in kinematic rupture models. *Geophysical Research Letters*, *31*, L04609. https://doi.org/10.1029/2003GL019225

Poli, P., & Prieto, G. A. (2016). Global rupture parameters for deep and intermediate-depth earthquakes. *Journal of Geophysical Research: Solid Earth*, *121*, 8871–8887. https://doi.org/10.1002/2016JB013521

Rice, J. R. (2006). Heating and weakening of faults during earthquake slip. *Journal of Geophysical Research*, *111*, B05311. https://doi.org/10.1029/2005JB004006

Rice, J. R., Lapusta, N., & Ranjith, K. (2001). Rate and state dependent friction and the stability of sliding between elastically deformable solids. *Journal of the Mechanics and Physics of Solids*, *49*(9), 1865–1898. https://doi.org/10.1016/S0022-5096(01)00042-4

Ruina, A. (1983). Slip instability and state variable friction laws. *Journal of Geophysical Research*, *88*(B12), 10,359–10,370. https://doi.org/10.1029/JB088iB12p10359

Ruiz, S., Madariaga, R., Astroza, M., Saragoni, G. R., Lancieri, M., Vigny, C., & Campos, J. (2012). Short-period rupture process of the 2010 M_w 8.8 Maule earthquake in Chile. *Earthquake Spectra*, *28*, S1–S18. https://doi.org/10.1193/1.4000039

Saffer, D. M., & Marone, C. (2003). Comparison of smectite- and illite-rich gouge frictional properties: Application to the updip limit of the seismogenic zone along subduction megathrusts. *Earth and Planetary Science Letters*, *215*(1-2), 219–235. https://doi.org/10.1016/S0012-821X(03)00424-2

Schmedes, J., Archuleta, R. J., & Lavallée, D. (2010). Correlation of earthquake source parameters inferred from dynamic rupture simulations. *Journal of Geophysical Research*, *115*, B03304. https://doi.org/10.1029/2009JB006689

Scholz, C. H. (1998). Earthquakes and friction laws. *Nature*, *391*(6662), 37–42. https://doi.org/10.1038/34097

Spudich, P., & Frazer, L. N. (1984). Use of ray theory to calculate high-frequency radiation from earthquake sources having spatially variable rupture velocity and stress drop. *Bulletin of the Seismological Society of America*, *74*(6), 2061–2082.

Sufri, O., Koper, K. D., & Lay, T. (2012). Along-dip seismic radiation segmentation during the 2007 M_w 8.0 Pisco, Peru earthquake. *Geophysical Research Letters*, *39*, L08311. https://doi.org/10.1029/2012GL051316

Tinti, E., Fukuyama, E., Piatanesi, A., & Cocco, M. (2005). A kinematic source-time function compatible with earthquake dynamics. *Bulletin of the Seismological Society of America*, *95*, 1211–1223. https://doi.org/10.1785/0120040177

VanDecar, J. C., & Crosson, R. S. (1990). Determination of teleseismic relative phase arrival times using multi-channel cross-correlation and least squares. *Bulletin of the Seismological Society of America*, *80*(1), 150–169.

Venkataraman, A., & Kanamori, H. (2004). Observational constraints on the fracture energy of subduction zone earthquakes. *Journal of Geophysical Research*, *109*, B05302. https://doi.org/10.1029/2003JB002549

Viesca, R. C., & Garagash, D. I. (2015). Ubiquitous weakening of faults due to thermal pressurization. *Nature Geoscience*, *8*(11), 875–879. https://doi.org/10.1038/ngeo2554

Wang, D., & Mori, J. (2011). Frequency-dependent energy radiation and fault coupling for the 2010 M_w 8.8 Maule, Chile, and 2011 M_w 9.0 Tohoku, Japan, earthquakes. *Geophysical Research Letters*, *38*, L22308. https://doi.org/10.1029/2011GL049652

Warren, L. M., & Shearer, P. M. (2000). Investigating the frequency dependence of mantle Q by stacking P and PP spectra. *Journal of Geophysical Research*, *105*(B11), 25,391–25,402. https://doi.org/10.1029/2000JB900283

Warren, L. M., & Shearer, P. M. (2002). Mapping lateral variations in upper mantle attenuation by stacking P and PP spectra. *Journal of Geophysical Research*, *107*(B12), 2342. https://doi.org/10.1029/2001JB001195

Warren, L. M., & Shearer, P. M. (2005). Using the effects of depth phases on *P*-wave spectra to determine earthquake depths. *Bulletin of the Seismological Society of America*, *95*(1), 173–184. https://doi.org/10.1785/0120030251

Xu, Y., Koper, K. D., Sufri, O., Zhu, L., & Hutko, A. R. (2009). Rupture imaging of the M_w 7.9 12 May 2008 Wenchuan earthquake from back projection of teleseismic *P* waves. *Geochemistry, Geophysics, Geosystems*, *10*, Q04006. https://doi.org/10.1029/2008GC002335

Yagi, Y., & Okuwaki, R. (2015). Integrated seismic source model of the 2015 Gorkha, Nepal, earthquake. *Geophysical Research Letters*, *42*, 6229–6235. https://doi.org/10.1002/2015GL064995

Yang, H., & Weng, H. (2016). Frictional properties and fracture energy constrained from frequency-dependent coseismic radiations of great earthquakes, AGU Fall Meeting, Abstract S12A-06

Yao, H., Gerstoft, P., Shearer, P. M., & Mecklenbräuker, C. (2011). Compressive sensing of the Tohoku-Oki M_w 9.0 earthquake: Frequency-dependent rupture modes. *Geophysical Research Letters*, *38*, L20310. https://doi.org/10.1029/2011GL049223

Yao, H., Shearer, P. M., & Gerstoft, P. (2012). Subevent location and rupture imaging using iterative back-projection for the 2011 Tohoku M_w 9.0 earthquake. *Geophysical Journal International*, *190*(2), 1152–1168. https://doi.org/10.1111/j.1365-246X.2012.05541.x

Yao, H., Shearer, P. M., & Gerstoft, P. (2013). Compressive sensing of frequency-dependent seismic radiation from subduction zone megathrust ruptures. *Proceedings of the National Academy of Sciences of the United States of America*, *110*(12), 4512–4517. https://doi.org/10.1073/pnas.1212790110

Ye, L., Lay, T., Kanamori, H., & Koper, K. D. (2015). Rapidly estimated seismic source parameters for the 16 September 2015 Illapel, Chile M_w 8.3 earthquake. *Pure and Applied Geophysics*, *173*(2), 321–332. https://doi.org/10.1007/s00024-015-1202-y

Ye, L., Lay, T., Kanamori, H., & Rivera, L. (2016). Rupture characteristics of major and great ($M_w \geq 7.0$) megathrust earthquakes from 1990 to 2015: 2. Depth dependence. *Journal of Geophysical Research: Solid Earth*, *121*, 845–863. https://doi.org/10.1002/2015JB012427

Yin, J., Yang, H., Yao, H., & Weng, H. (2016). Coseismic radiation and stress drop during the 2015 M_w 8.3 Illapel, Chile megathrust earthquake. *Geophysical Research Letters*, *43*(4), 1520–1528. https://doi.org/10.1002/2015GL067381

Yin, J., & Yao, H. (2016). Rupture and frequency-dependent seismic radiation of the 2012 M_w 8.6 Sumatra strike-slip earthquake. *Geophysical Journal International*, *205*(3), 1682–1693. https://doi.org/10.1093/gji/ggw105

Yin, J., Yao, H., Yang, H., Qin, W., Jing, L.-Z., & Zhang, H. (2017). Frequency-dependent rupture process, stress change, and seismogenic mechanism of the 25 April 2015 Nepal Gorkha M_w 7.8 earthquake. *Science China Earth Sciences*, *60*(4), 796–808. https://doi.org/10.1007/s11430-016-9006-0

Yue, H., Castellanos, J. C., Yu, C., Meng, L., & Zhan, Z. (2017). Localized water reverberation phases and its impact on back-projection images. *Geophysical Research Letters*, *44*(19), 9573–9580. https://doi.org/10.1002/2017GL073254

Yue, H., Simons, M., Duputel, Z., Jiang, J., Fielding, E., Liang, C., … Samsonov, S. V. (2016). Depth varying rupture properties during the 2015 M_w 7.8 Gorkha (Nepal) earthquake. *Tectonophysics*, *714-715*, 44–54. https://doi.org/10.1016/j.tecto.2016.07.005